Geochemistry Geophysics Geosystems G3

Article
Volume 13, Number 1
29 September 2012
Q0AO02, doi:10.1029/2012GC004146
ISSN: 1525-2027

Published by AGU and the Geochemical Society

Signatures and significance of aeolian, fluvial, bacterial and diagenetic magnetic mineral fractions in Late Quaternary marine sediments off Gambia, NW Africa

Janna Just
MARUM – Center for Marine and Environmental Sciences and Faculty of Geosciences, University of Bremen, PO Box 330440, DE-28334 Bremen, Germany (janna.just@uni-bremen.de)

Mark J. Dekkers
Paleomagnetic Laboratory "Fort Hoofddijk," Department of Earth Sciences, Faculty of Geosciences, Utrecht University, Budapestlaan 17, NL-3584 CD Utrecht, Netherlands (m.j.dekkers@uu.nl)

Tilo von Dobeneck
MARUM – Center for Marine and Environmental Sciences and Faculty of Geosciences, University of Bremen, PO Box 330440, DE-28334 Bremen, Germany (dobeneck@uni-bremen.de)

Annelies van Hoesel
Structural Geology and Tectonics, Department of Earth Sciences, Faculty of Geosciences, Utrecht University, Budapestlaan 4, NL-3584 CD Utrecht, Netherlands (a.vanhoesel@uu.nl)

Torsten Bickert
MARUM – Center for Marine and Environmental Sciences and Faculty of Geosciences, University of Bremen, PO Box 330440, DE-28334 Bremen, Germany (tbickert@marum.de)

[1] Two gravity cores retrieved off NW Africa at the border of arid and subtropical environments (GeoB 13602–1 and GeoB 13601–4) were analyzed to extract records of Late Quaternary climate change and sediment export. We apply end-member (EM) unmixing to 350 acquisition curves of isothermal remanent magnetization (IRM). Our approach enables to discriminate rock magnetic signatures of aeolian and fluvial material, to determine biomineralization and reductive diagenesis. Based on the occurrence of pedogenically formed magnetic minerals in the fluvial and aeolian EMs, we can infer that goethite formed in favor to hematite in more humid climate zones. The diagenetic EM dominates in the lower parts of the cores and within a thin near-surface layer probably representing the modern Fe^{2+}/Fe^{3+} redox boundary. Up to 60% of the IRM signal is allocated to a biogenic EM underlining the importance of bacterial magnetite even in siliciclastic sediments. Magnetosomes are found well preserved over most of the record, indicating suboxic conditions. Temporal variations of the aeolian and fluvial EMs appear to faithfully reproduce and support trends of dry and humid conditions on the continent. The proportion of aeolian to fluvial material was dramatically higher during Heinrich Stadials, especially during Heinrich Stadial 1. Dust export from the Arabian-Asian corridor appears to vary contemporaneous to increased dust fluxes at the continental margin of NW Africa emphasizing that meltwater discharge in the North Atlantic had an enormous impact on atmospheric dynamics.

Components: 13,700 words, 9 figures, 2 tables.

Keywords: IRM end-member modeling; NW Africa; environmental magnetism; magnetotactic bacteria; paleoclimate; terrigenous input.

Index Terms: 1512 Geomagnetism and Paleomagnetism: Environmental magnetism; 1605 Global Change: Abrupt/rapid climate change (4901, 8408); 1622 Global Change: Earth system modeling (1225, 4316).

Received 14 March 2012; **Revised** 16 August 2012; **Accepted** 21 August 2012; **Published** 29 September 2012.

Just, J., M. J. Dekkers, T. von Dobeneck, A. van Hoesel, and T. Bickert (2012), Signatures and significance of aeolian, fluvial, bacterial and diagenetic magnetic mineral fractions in Late Quaternary marine sediments off Gambia, NW Africa, *Geochem. Geophys. Geosyst.*, *13*, Q0AO02, doi:10.1029/2012GC004146.

Theme: Magnetism From Atomic to Planetary Scales: Physical Principles and Interdisciplinary Applications in Geosciences and Planetary Sciences

1. Introduction

[2] Over the past twenty years, rock magnetic methods have been increasingly used to distinguish sources of terrigenous sediment fractions in marine sediments. *Bloemendal et al.* [1988, 1992] were the first to map the distribution of magnetic minerals in the eastern equatorial Atlantic Ocean and to identify specific magnetic mineral fractions with their terrigenous source or diagenetic formation processes. They observed that Saharan dust contains high abundances of antiferromagnetic (hematite and goethite) versus ferrimagnetic (magnetite and maghemite) minerals. A widely distributed ultrafine magnetite fraction varying on glacial-interglacial timescales was tentatively associated with either fluvial input or post-depositional bacterial biomineralization [*Bloemendal et al.*, 1988, 1992].

[3] *Schmidt et al.* [1999] presented a fuzzy c-means cluster analysis based on magnetic properties of 194 core top samples collected from all parts of the South and Equatorial Atlantic. They distinguished rock magnetic provinces, each defined by a characteristic lithogenic or biogenic magnetic signature and assigned nearby deserts, rivers, volcanoes and mid-ocean ridges as source areas. Magnetic fingerprints of terrigenous sediment fractions have been identified and exploited by several multiproxy studies. *Larrasoaña et al.* [2003] and *Köhler et al.* [2008] combined rock magnetic and geochemical methods to analyze Neogene Mediterranean sediments and interpreted elevated hematite and titanium contents as indices of enhanced north Saharan dust supply and hence of greater aridity.

[4] *Itambi et al.* [2009, 2010] investigated marine rock magnetic records off Senegal and Gambia to reconstruct southward shifts of the Intertropical Convergence Zone (ITCZ) concurrent with North Atlantic Heinrich events during the respective Heinrich stadials (HS) [*Mulitza et al.*, 2008], which were responsible for arid conditions in N Africa. In line with earlier *Bloemendal et al.* [1988, 1992] studies, *Itambi et al.* [2009, 2010] noted that hematite and goethite occurred mainly during more arid glacial and stadial periods and should consequently be of aeolian origin. Very fine-grained and generally ubiquitous magnetite present throughout their records was interpreted as fluvial input associated with more humid periods on the African continent. The magnetic expression of HS 1 is much stronger with respect to the remaining HSs, while HS 3 is less pronounced in their southernmost records. There is clear and acknowledged evidence for iron oxide reduction in the lower parts of these cores [*Itambi et al.*, 2009], but it remains uncertain to what extent bacterial magnetite has contributed to the magnetic fine fraction of modern and past ocean margin sediments offshore NW Africa.

[5] Bacterial magnetite is often considered a subordinate or negligible magnetic mineral phase in oceanic regions with high terrigenous input. However, it has also been described as an abundant or even dominant magnetic mineral phase in the surficial sediments of upwelling regions off SW Africa [e.g., *Schmidt et al.*, 1999; *Hilgenfeldt*, 2000]. Unjustified disregard of bacterial magnetite or its incorrect distinction from fluvial magnetite phases necessarily leads to erroneous conclusions concerning continental humidity and runoff. Interpretation of the terrigenous fraction of marine sediments off NW Africa is further complicated by the existence of various potential dust sources and wind systems. It has been claimed that NE trade winds export more local (coastal) Sahelian and Saharan dust to sea,

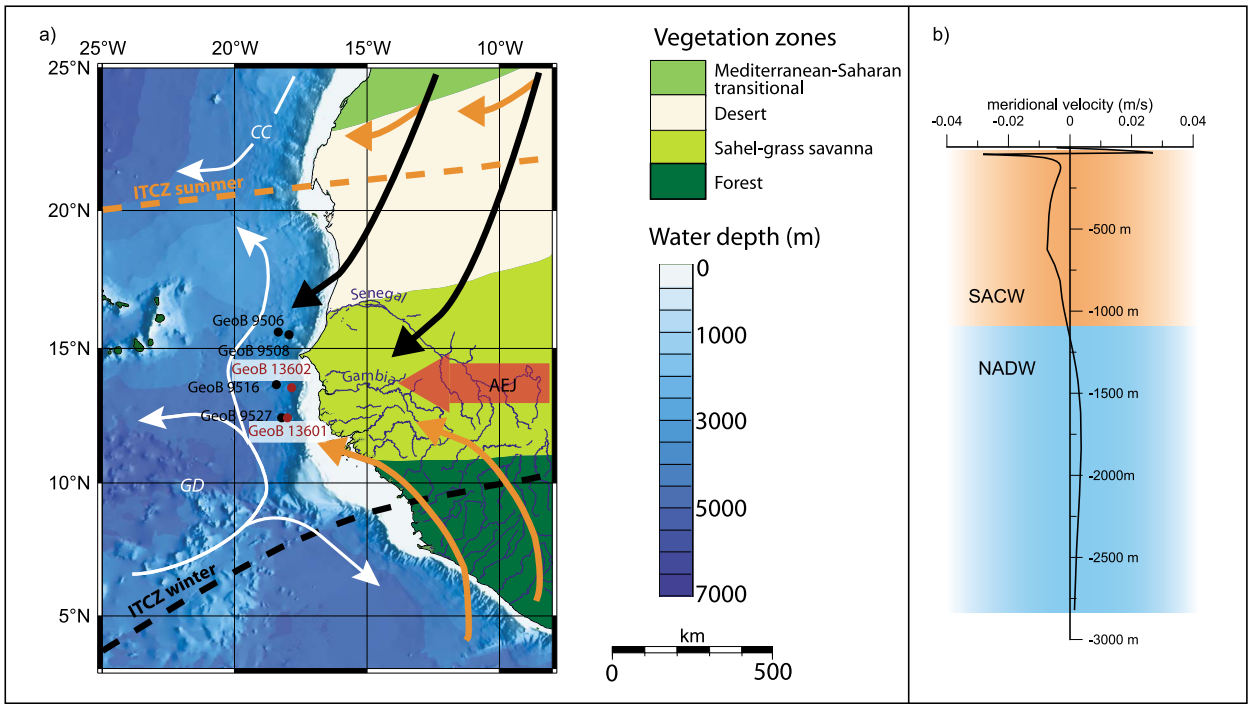

Figure 1. (a) Vegetation belts in NW Africa modified after *White* [1983]. Dust export to the NW continental margin from the proximal Sahara and Sahel occurs mainly during winter by the NE Trade winds (black arrows) while the Inter Tropical Convergence Zone (ITCZ) is located to the south. Dust is transported by the African Easterly Jet (AEJ) at high altitudes (~3000 m). During summer, the SE Trades (orange arrows) and the associated monsoon system are responsible for rainfall in the Sahel. Surface water circulation in the south is controlled by the Equatorial Counter Current and associated anticyclonic circulation around the Guinea Dome (*GD*) and in the north by the Canary Current (*CC*), here indicated by white arrows. The gravity cores studied here are depicted in red. Gravity cores referred to in this study are indicated in black. (b) Vertical profile of meridional current velocities ECCO/JPL data assimilating model kf080 (http://grace.jpl.nasa.gov/data/ECCOOBP/). Positive and negative numbers indicate southward and northward flow, respectively. SACW: South Atlantic Central Water, NADW: North Atlantic Deep Water.

while the African Easterly Jet (AEJ) releases dust from more distant Central Saharan sources which is further transported over the Atlantic within the Saharan Air Layer [e.g., *Pye*, 1987; *Chiapello et al.*, 1995]. Not all studies, however, make this distinction, and little evidence for separate dust sources in rock magnetic or geochemical marine records has been shown so far.

[6] The studies of *Bloemendal et al.* [1988, 1992] and *Itambi et al.* [2009] have established that the magnetic mineralogy may be used to identify humid and arid phases in NW Africa. In order to budget aeolian and fluvial sediment input, however, the magnetic inventory of these fractions must be quantified and the imprint of biomineralization and diagenetic processes must be determined.

[7] In several other recent rock magnetic provenance studies [e.g., *Hounslow and Morton*, 2004; *Heslop and Dillon*, 2007; *Maher et al.*, 2009; *Roberts et al.*, 2011b], isothermal remanent magnetization (IRM) acquisition curves serve as input for mathematically unmixing of sediments into their source components. IRM acquisition curves provide a concentration-dependent numerical representation of the full coercivity spectrum, and, accordingly, of the entire magnetic mineral population of given sedimentary mixtures. They obey the principles of linear mixing systems and are therefore suitable for application of end-member (EM) modeling techniques [*Egli*, 2004b; *Heslop and Dillon*, 2007].

[8] Two suitable sites on the continental rise at the western border of arid subtropical and humid tropical NW Africa have been selected (Figure 1a) to determine such end-members: Site GeoB 13602 is located slightly north of the present Gambia River mouth while site GeoB 13601 is situated 100 km further south. Magnetic characteristics and mineralogy of each obtained EM are subsequently analyzed by Cumulative Log-Gaussian (CLG) IRM component fitting [*Kruiver et al.*, 2001], thermomagnetic measurements and electron microscopy. Together these data provide a quantitative system to

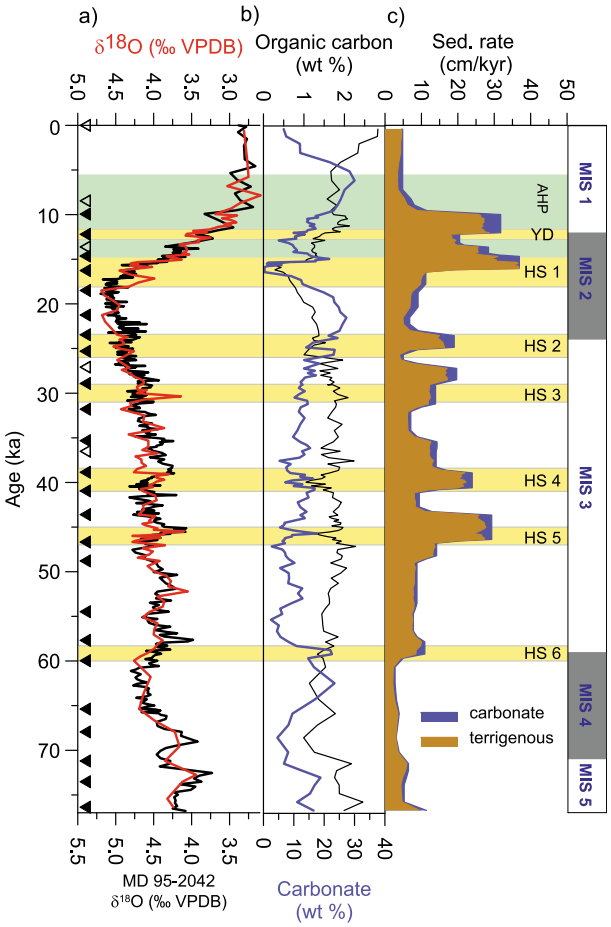

Figure 2. (a) Oxygen isotope records for cores MD 95–2042 (black) [*Shackleton et al.*, 2000] and GeoB 13602–1 (red). Filled triangles indicate the ages derived by correlating the benthic $\delta^{18}O$ records and open triangles mark calibrated radiocarbon ages. (b) Weight % of total organic carbon and $CaCO_3$ of GeoB 13602–1. (c) Sedimentation rate split into biogenic and terrigenous fractions based on carbonate weight % and assumed equal dry bulk density of both fractions. Low sedimentation rates at the bottom of the core are most probably due to sediment compaction during coring. MIS: Marine Isotope Stage, AHP: African Humid Period (light green), YD: Younger Dryas, HS: Heinrich Stadial (adopted from *Sarnthein et al.* [2001]), LGM: Last Glacial Maximum.

discriminate aeolian, fluvial, bacterial, and diagenetic magnetic mineral associations.

2. Geological and Hydrographic Setting

[9] The continental margin off Gambia (NW Africa, Figure 1a) is composed of an approximately 100 km wide and up to 400 m deep shelf and a continental slope descending at an angle of about 2.5° to water depths of 3000 m. From the north, the study area is under marginal influence of the westward turning Canary Current, which is fed by the easternmost branch of the Azores Current [*Knoll et al.*, 2002]. From the south, the seasonal cyclonic circulation around the Guinea Dome influences the study area, inducing a northward transport of surface water. The convergence of this gyre and the Canary current marks the boundary of North Atlantic Central Water and South Atlantic Central Water [*Tomczak*, 2003]. The northward-directed surface current of the South Atlantic Central Water entrains the upper 300–600 m of the water column in the study area. Underneath is the southward-directed North Atlantic Deep Water (NADW; 1000–4000 m) [*Tomczak*, 2003]. The velocity profile of both meridional currents (Figure 1b) reveals that the net transport of suspended material is to the north. Accordingly, satellite images (public data from Naval Research Laboratory, http://www7320.nrlssc.navy.mil/GLBhycom1-12/equatl.html) and modeled surface currents [*Mittelstaedt*, 1991] indicate that the freshwater plume and hence the sediment load of the Gambia River is primarily deflected toward the northern site. Aeolian material from the Sahara and Sahel is transported to both sites by NE winter monsoons at lower atmospheric altitude and by the higher AEJ [*Pye*, 1987; *Stuut et al.*, 2005; *Mulitza et al.*, 2008].

3. Materials and Chronology

[10] The studied gravity cores GeoB 13602–1 (position: 13°32.71′N; 17°50.96′W, water depth: 2395 m, core length: 8.75 m) and GeoB 13601–4 (position: 12°26.06′N, 18°00.29′W, water depth: 2997 m, core length 8.55 m) were retrieved in 2009 during RV *Maria S. Merian* cruise MSM 11/2 on the continental slope. Both cores mainly consist of siliciclastic, dark olive clays and silts.

[11] To estimate the amount of biogenic content within the cores, GeoB 13602–1 samples were analyzed for biogenic opal (always < 2.5%, data not shown), total carbon and total organic carbon using an Elementar Vario EL III analyzer. $CaCO_3$ weight percentages are calculated on this basis. Carbonate content is generally lower than 25 wt % and organic carbon ranges between 2.5% in the uppermost parts of the core and 0.5% during HS 1 (Figure 2b).

[12] GeoB 13602–1 was sampled at 5 cm intervals, from which specimens of the epibenthic species *Cibicoides wuellestorfi* were picked for stable isotope analyses (performed with a Finnigan MAT 252 mass spectrometer). The age model was obtained by correlating the oxygen isotope record (Figure 2a) to that of core MD 95–2042 [*Shackleton et al.*, 2000].

Table 1. Radiocarbon Data for Core GeoB 13602–1

Depth in Core (cm)	Sample Code	^{14}C Age (^{14}C a BP)	Calender Age (a BP)	1σ Calender Age Range (a BP)
2	Poz-35102	*modern*	*modern*	*modern*
41	Poz-41307	7990 ± 70	8454	8380-8521
101	Poz-41304	10890 ± 70	12404	12175-12595
154	Poz-41305	12200 ± 70	13619	13483-13729
221	Poz-35103	12790 ± 60	14403	14103-14567
352	Poz-41306	22800 ± 140	27084	27536-27189
480	Poz-41309	32400 ± 600	36511	35470-37203

From six samples at depths of 0.02 m, 0.41 m, 1.01 m, 1.54 m, 2.21 m, 3.52 m, 4.50 m, planktonic foraminifera tests of *G. ruber, G. saculifer, G. bulloides* and *G. inflata* were selected for radiocarbon analysis with a 1.5 SDH-Pelletron Model Compact Carbon AMS at the Poznań Radiocarbon Laboratory. Assuming a reservoir age of 400 years, raw ^{14}C ages (Table 1) were converted into calendar ages using the calibration curve of *Reimer et al.* [2009]. Inclusion of ^{14}C ages from depths of 1.01 m and 2.21 m taken within the Younger Dryas and HS 1 intervals would lead to a misfit with the oxygen isotope records. Since meltwater discharge during these periods led to changes in NADW production [e.g., *Stocker and Wright*, 1991; *Broecker*, 1998] and thus to possible ingressions of southern ocean waters with a different reservoir age, we excluded these ^{14}C ages. A small scale turbidite at 3.90–4.00 m depth was excluded for the age-model construction. The age model of core GeoB 13602–1 was then transferred to core GeoB 13601–4 by correlating their diffuse reflectance spectrophotometry records (data not shown) and rock magnetic parameters. GeoB 13602–1 spans the past 76 ka with a mean sedimentation rate of 11.5 cm/kyr while GeoB 13601–4 spans the past 60 ka with a mean sedimentation rate of 14 cm/kyr. On the basis of the carbonate weight, sedimentation rates for GeoB 13602–1 were calculated for the biogenic and terrigenous fractions (Figure 2c) assuming the same dry bulk density for both fractions.

4. Methods

4.1. Rock Magnetism

4.1.1. Room Temperature Magnetic Measurements

[13] For both cores, rock magnetic properties were measured on 6.2 cm^3 samples taken at 5 cm spacings (~400 samples). Low-field magnetic susceptibility (χ) was determined using a Kappabridge KLY-2 susceptometer (measurement frequency 920 Hz). Frequency dependence of susceptibility (χ_{fd}), which serves as a measure of the presence of ultra-fine superparamagnetic (SP) magnetite [*Dearing et al.*, 1996] was measured for GeoB 13602–1 using a Bartington Instruments MS2B meter. Measurements of laboratory-induced remanence parameters were performed using an automated 2-G Enterprises 755R DC superconducting magnetometer. Anhysteretic remanent magnetization ($ARM_{100\ mT}$) which indicates the presence of fine-grained single domain (SD) magnetite [*King et al.*, 1982; *Frederichs et al.*, 1999] was induced with a 100 mT AF and a 40 μT DC bias field. IRM acquisition curves, cumulative coercivity distributions of the integral magnetic mineral assemblage [e.g., *Eyre*, 1996; *Frank and Nowaczyk*, 2008], were obtained using an in-line pulse magnetizer and an "external" pulse magnetizer (2-G Enterprises). For a more detailed description of the experimental setup, see auxiliary material.[1] We use the magnetic remanence acquired at 100 mT ($IRM_{100\ mT}$) to estimate the multidomain (MD) magnetite content [*Frederichs et al.*, 1999]. $ARM_{100\ mT}/IRM_{100\ mT}$ can thus be used as a magnetic grain-size indicator. The S-Ratio, $S = 0.5[(-IRM_{(-300\ mT)}/SIRM) + 1]$, represents the ratio of low to high-coercivity magnetic minerals [*Bloemendal et al.*, 1992]. The hard IRM (HIRM) [*Stoner et al.*, 1996], $HIRM = 0.5(SIRM + IRM_{(-300\ mT)})$ quantifies high-coercivity magnetic minerals [*Frederichs et al.*, 1999; *Kruiver and Passier*, 2001; *Heslop*, 2009].

4.1.2. Low- and High-Temperature Magnetic Measurements

[14] High- and low-temperature magnetic measurements were performed on selected dry bulk samples. Low-temperature cycling experiments between 5 and 300 K (2 K steps) were conducted with a Quantum Design XL7 Magnetic Properties Measurement System (MPMS) at Bremen

[1]Auxiliary materials are available in the HTML. doi:10.1029/2012GC004146.

University (Germany). We measured warming curves after zero-field cooling (ZFC) and after in-field cooling (FC). SIRM warming experiments were performed in a temperature interval of 240–400 K (see auxiliary material for a detailed description). High-temperature measurements of magnetization versus temperature were made in air between 25 and 700°C on a modified horizontal translation Curie balance (*Mullender et al.* [1993], cycling field 20–400 mT), heating and cooling rates were 10°C/min.

4.2. Scanning and Transmission Electron Microscopy

[15] Scanning electron microcope (SEM) and transmission electron microscope (TEM) observations were performed on heavy-liquid and magnetic separates (description of the sample preparation, see auxiliary material). For SEM observations, the specimens were gold-coated and analyzed on a SUPRA TM 40 high-resolution Field Emission SEM instrument at the Institute of Historical Geology – Paleontology at Bremen University. For imaging, the secondary electron (SE) beam was used at energy levels between 5 and 15 keV. To obtain the elemental composition of the particles, energy dispersive spectroscopy (EDS) with an energy level of 15 keV was performed.

[16] Transmission electron microscope images were gathered with a FEI Tecnai 20 FEG TEM at the Electron Microscope Centre (Utrecht University), operated in bright field mode with an acceleration voltage of 200 keV. Diffraction patterns have also been analyzed. All shown EDS spectra are normalized to oxygen maxima.

4.3. Numerical Unmixing

[17] In a mathematical sense, remanence-based sedimentary magnetic records constitute linear combinations of the respective magnetic properties of all contributing source or mineral fractions. End-member (EM) analysis is an inverse technique aimed at numerically unmixing such components. It assumes that a composite record consists of a small, discrete and a priori unknown number of geologically independent and magnetically distinguishable components, whose properties remain constant over time. EM analysis yields a minimal set of EM curves, whose properties best explain the full internal variability of a data set. Basis functions are not needed and the only criterion for the input curves is monotony. To further characterize the magnetic properties of calculated EMs, IRM component analysis [*Kruiver et al.*, 2001] has been applied. This is, in contrast, a forward technique and requires a system of hypothetical basis functions. Multiple cumulative log Gaussian (CLG) basis functions are used to fit the bulk signal [cf. *Robertson and France*, 1994]. Because of the different nature of these techniques (inverse and forward), they can be run in conjunction for mutual verification.

4.3.1. End-Member Analysis

[18] All IRM acquisition curves were unmixed using the IRM Unmixer code by *Heslop and Dillon* [2007], which adopts the algorithm developed by *Weltje* [1997]. In the fundamental equation of EM analysis, $\boldsymbol{X} = \boldsymbol{AS} + \boldsymbol{\epsilon}$, $\boldsymbol{X}$ represents a $n*m$ matrix of n observations (=individual samples) in rows and m variables (=IRM steps) in columns. $\boldsymbol{A}$ denotes the abundance of a set of k EMs in columns for the n samples in rows, $\boldsymbol{S}$ represents the m properties of the k EMs, and $\boldsymbol{\epsilon}$ is the error matrix. Because the contributions of each EM must be positive, a non-negativity constraint ($\boldsymbol{A_{ij}} \geq 0$) is included in the EM algorithm [*Heslop and Dillon*, 2007; *Heslop et al.*, 2007]. Error sources are instrumental noise and temporal variations of individual source signatures. The decision on how many EMs to include is a compromise between keeping the number of components as low as possible while having a reasonable correlation of modeled and input data. IRM Unmixer provides decision criteria by performing principal component analysis (PCA) with increasing numbers of components and returning their coefficients of determination (R^2). EMs should be geologically interpretable within their environmental settings [*Prins*, 1999; *Weltje and Prins*, 2007]. Note that the contribution of each EM ($\boldsymbol{A}$) refers to its SIRM and cannot directly be translated to volume or mass percentages. A volume calibration of magnetic EMs would require detailed information about (a) the concentration of magnetic minerals in the bulk sedimentary EMs and (b) the geochemistry and crystal structure of the respective minerals.

4.3.2. IRM Component Analysis

[19] To assess the magnetic mineralogy of the EMs, IRM component analysis has been applied on the IRM acquisition curves that emerge from the EM unmixing. IRM acquisition curves of a mixed magnetic mineralogy can be described as a combination of different CLGs [*Robertson and France*, 1994] $\boldsymbol{s} = \boldsymbol{Cb} + \boldsymbol{\epsilon}$, where $\boldsymbol{s}$ represents the measured (or modeled) IRM acquisition curve, $\boldsymbol{C}$ denotes the IRM acquisition curves of the components and $\boldsymbol{b}$ the proportion of each component to SIRM. CLG components are

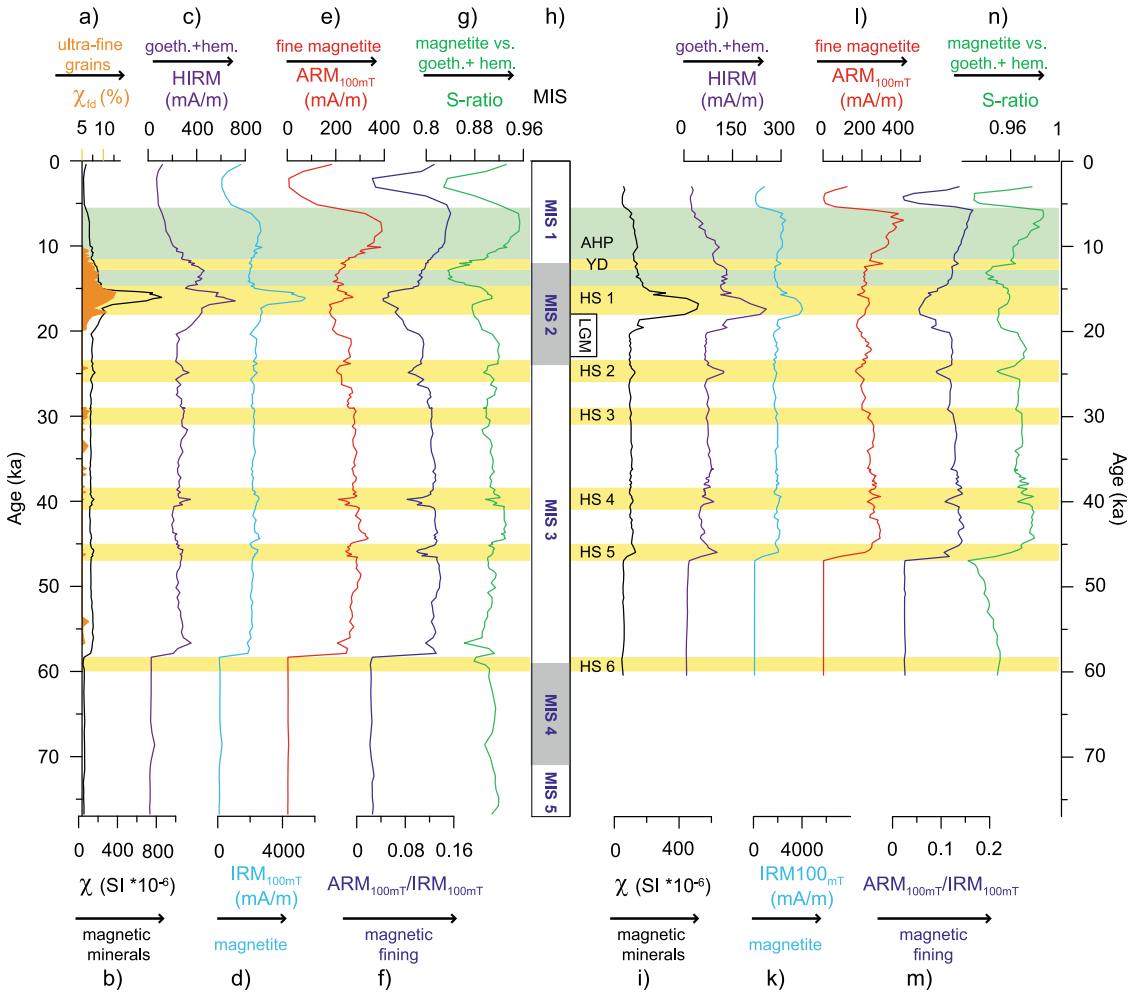

Figure 3. Rock magnetic record for (a–g) GeoB 13602–1 and (i–n) GeoB 13601–4. (h) Marine Isotope Stages (MIS) are depicted in this panel. AHP: African Humid Period (light green), YD: Younger Dryas, HS: Heinrich Stadial, LGM: Last Glacial Maximum.

characterized by their magnitude (corresponding to SIRM contribution), median field $B_{1/2}$ (at which half of the SIRM of the component is acquired) and dispersion parameter DP (reflecting the width of the coercivity distribution which in log space is equivalent to one standard deviation). The approach used here has been developed by *Kruiver et al.* [2001]. For further details, see *Kruiver et al.* [2001] and *Heslop et al.* [2004]. The IRM acquisition curves can depart from log Gaussian functions due to thermal effects, magnetic interaction [*Egli*, 2003] as well as the starting state of the magnetic system [*Petrovský et al.*, 1993; *Heslop et al.*, 2004], which should be taken into account when performing the curve fitting. Estimates of components relate to their magnetic moment, which cannot be converted directly into magnetic mineral concentrations, e.g., the SIRM of magnetite is 1–20 Am^2kg^{-1} (grain size dependent) and is thus ~200 times higher than for hematite (0.08–0.2 Am^2kg^{-1}) and goethite (0.02–0.1 Am^2kg^{-1}) [*Peters and Dekkers*, 2003].

5. Results

5.1. Room Temperature Magnetic Measurements

5.1.1. Core GeoB 13602–1

[20] The lowermost interval of GeoB 13602–1 from 76 to 57 ka (8.75–7.80 m depth) is marked by quasi-absence of magnetic minerals in the fine SD (Figure 3e) and coarser MD (Figure 3d) fractions. Since the loss of ARM is strongest, the relict phase is coarser (Figure 3f) than the pristine. A similar pattern is found in the shallow interval of 4.1–1.2 ka (0.35–0.20 m depth). These conspicuous differences and the sharp boundaries with the remaining

part of the records indicate that pervasive reductive diagenesis of the primary iron oxides has affected both intervals [e.g., *Karlin and Levi*, 1983; *Garming et al.*, 2005; *Rowan et al.*, 2009]. The apparently well-preserved remainder of the record from 57 to 4.1 ka has relatively stable values except for shorter intervals that correspond to HSs. A coarsening of the magnetic grain size (Figure 3f), and an absolute increase of high-coercivity magnetic minerals (i.e., hematite and/or goethite, Figure 3c) with related S-ratio minima is observed in the intervals of HS 5, HS 4 and HS 2. Prominent peaks in χ, χ_{fd}, HIRM, IRM_{100mT}, and troughs of ARM_{100mT}/IRM_{100mT} exist during HS 1. A minimum and successive maximum of the S-ratio (Figure 3g) after 16.4 ka implies changes in the balance of high- to low-coercivity magnetic minerals and an increase of fine-grained magnetite (Figure 3e). Around 12.5 ka, during the Younger Dryas (YD), less pronounced maxima and minima occur, followed by increasing magnetite concentration of SD magnetite (Figure 3e), accompanied by a fining magnetic grain size (Figure 3f).

5.1.2. Core GeoB 13601–4

[21] The magnetic record of core GeoB 13601–4 largely matches that of GeoB 13602–1. An equally radical loss in magnetic minerals is present in the lowermost interval from 60 to 45 ka (8.55–7.50 m). Furthermore, the interval from 6 to 3 ka (0.40–0.20 m depth) is partly depleted in magnetic minerals. The intermediate interval from 45 ka to 6 ka has relatively small (10–20%) variations in all magnetic signals. Local deviations during HS 4 and HS 2 imply a relative increase of coarser magnetite grains (Figure 3m), as well as high-coercivity minerals (Figure 3j). During HS 1, χ, HIRM and IRM_{100mT} peak, whereas the S-ratio and ARM_{100mT}/IRM_{100mT} have minima. Another local minimum during the Younger Dryas (12.5 ka) is only evident in the S-ratio (Figure 3n).

5.1.3. Comparison of Cores GeoB 13602–1 and GeoB 13601–4

[22] Magnetic parameters for the northern core GeoB 13602–1 are approximately 20% (χ,), 35% (HIRM), 20% (IRM_{100mT}), and 10% (ARM_{100mT}) higher with respect to those of the southern core GeoB 13601–4. In particular, the high-coercivity mineral fraction (hematite and goethite) is more abundant at the northern site. All HS peaks in the northern core are also more pronounced. While other peaks in both cores largely correspond, the maximum at HS 5 in GeoB 13602–1 has no counterpart in the southern core. Note, however, that in GeoB 13601–4, HS 5 is located just above the diagenetic zone. The most prominent peak in both records corresponds to HS 1. Peaks in magnetic parameters that coincide with North Atlantic Heinrich Events have been previously reported from the nearby gravity cores GeoB9516–5 and GeoB9527–5 [*Itambi et al.*, 2009] (cf. Figure 1a) and were interpreted as periods of massive dust export and thus arid continental conditions in NW Africa. According to this interpretation, our record indicates that aeolian sediments contain a higher amount of coarse-grained magnetite, goethite and/or hematite, and a higher content of ultra-fine SP magnetite and/or maghemite. The latter correspond most likely to pedogenically formed coatings on silicate grains [*Sarnthein et al.*, 1981; *Itambi et al.*, 2009, *Lyons et al.*, 2010].

5.2. End-Member Analysis

[23] EM analyses for the individual cores and the pooled data set have been compiled in Figure 4. For the southern core GeoB 13601–4, three EMs ($S1_S$, $S2_S$ and $S3_S$) suffice to reach a high coefficient of determination (R^2 = 0.97, Figure 4a). To unmix the northern GeoB 13602–1 record, four EMs ($S1_N$, $S2_N$, $S3_N$, $S4_N$) were selected (R^2 = 0.97, Figure 4a), although three EMs also yield a reasonable R^2 of 0.96 at the break in slope of the R^2 plot. However, as will be shown later, large similarities between three of the four EMs for GeoB 13602–1 and the three EMs for GeoB 13601–4 justify a consideration of four EMs in the former. Four EMs (***S1***, ***S2***, ***S3***, ***S4***) were also used to fit the merged data sets of both cores (R^2 = 0.97).

[24] The absolute contributions of modeled EMs to SIRM are shown in Figures 4d–4g, while the outer panels (Figures 4b, 4c, 4h, and 4i) are plots of their respective IRM acquisition curves. Note that Figures 4h and 4i contain the EMs ***S1***–***S4*** derived from the merged data set as well as those from the individual northern ($S1_N$–$S4_N$) and southern cores ($S1_S$–$S3_S$), respectively, which are depicted in gray for comparison. There are strong similarities between $S1_N$, $S2_N$, $S3_N$ and $S4_N$ and ***S1***, ***S2***, ***S3***, ***S4*** (Figure 4h), while the EMs from the southern core $S1_S$, $S2_S$ and $S3_S$ resemble ***S1***, ***S3*** and ***S4*** (Figure 4i).

5.2.1. GeoB 13602–1

[25] The magnetically depleted lowermost interval of core GeoB 13602–1 (cf. Figure 3) is marked by significant drop of SIRM, exclusively $S4_N$ and $S3_N$ are present. While the contribution of $S4_N$ remains relatively stable throughout the record, the contribution

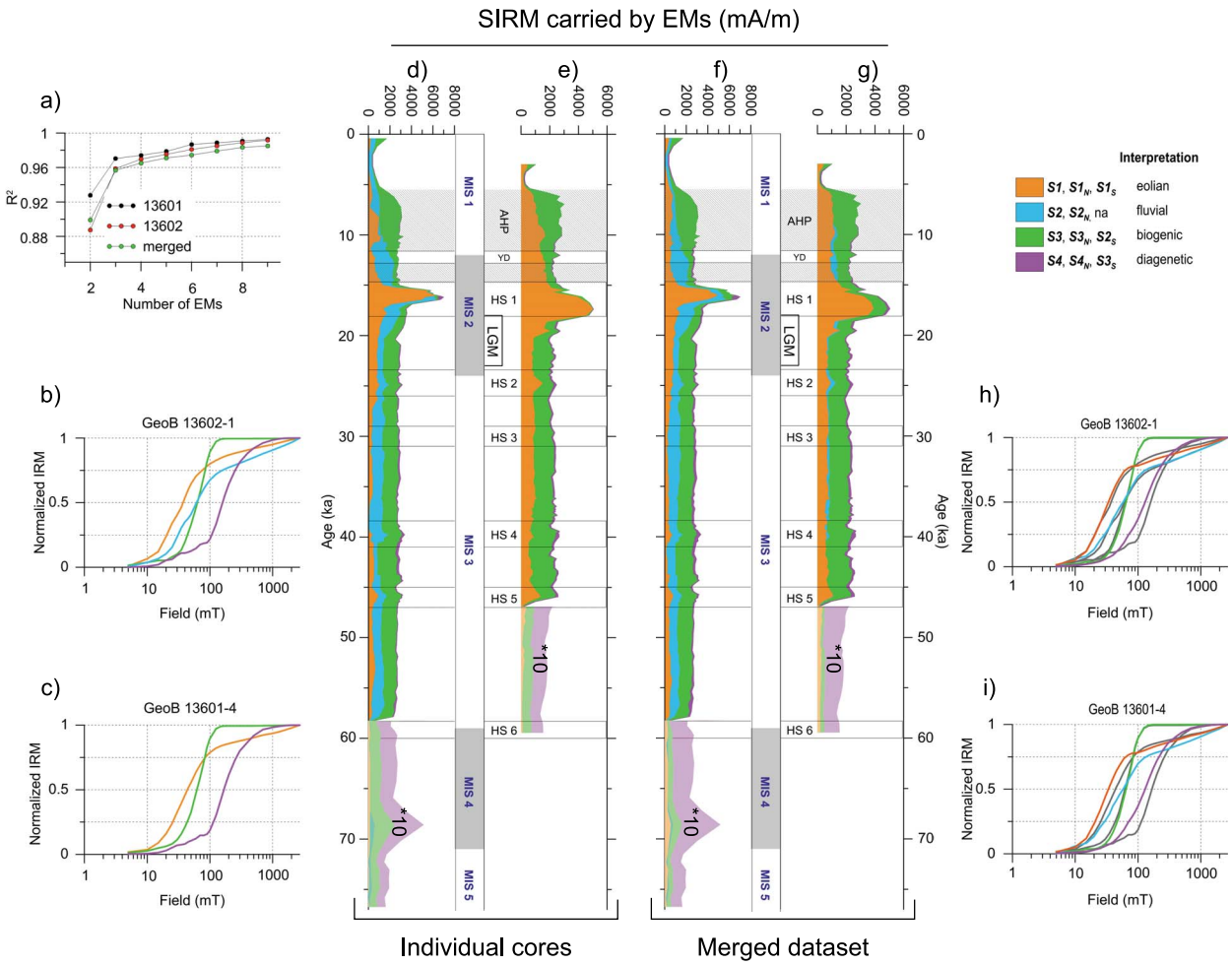

Figure 4. Results of end-member unmixing. (a) Coefficient of determination (R^2) for increasing numbers of EMs for individual cores and merged data sets. Results from individual cores: IRM acquisition curves of EMs for cores (b) GeoB 13602–1, and (c) GeoB 13601–4. Down-core contributions of EMs in cores (d) GeoB 13602–1 and (e) GeoB 13601–4. Results from merged data set: down-core contribution of EMs in cores (f) GeoB 13602–1 and (g) GeoB 13601–4. Note that in the lower intervals of the cores, the SIRM carried by the EMs are scaled by a factor of 10. (h, i) IRM acquisition curves of EMs of merged data set compared to EMs derived from individual data sets (gray shadings).

of $S3_N$ rises rapidly above the diagenetically affected interval. In the interval 58–26 ka, $S1_N$, $S2_N$, and $S3_N$ are present with relatively stable contributions to SIRM of 15–25%, 20–30% and 40–50%, respectively. $S1_N$ has minor peaks at 53.5 and 46.2 ka (the latter is HS 5). During HS 2 and the LGM, the relative proportion of $S1_N$ increases at the cost of all other EMs and reaches a dominant peak during HS 1. Above this peak, its impact decreases and $S2_N$ peaks at 14.2–12.5 ka (first part of the African Humid Period). At 8.5 ka the contribution of $S3_N$ has a high contribution, accounting for 60% of the SIRM.

5.2.2. GeoB 13601–4

[26] The magnetically depleted zone in core GeoB 13601–4 below 46 ka and the narrow diagenetic layer near the core top (cf. Figure 3) are equally indicated by the presence of $S3_S$ (Figure 4e) and $S2_S$. From 46 to 21.2 ka, the variations of the $S1_S$ and $S2_S$ are low, however, an increasing trend of $S1_S$ is observed. Local peaks of $S1_S$ occur during HS 5 and HS 2. During HS 1, $S1_S$ reaches a contribution of nearly 100% to SIRM and remains dominant until about 13 ka. Above, the proportion of $S1_S$ decreases while the contribution of $S2_S$ rises with a maximum at 6.8 ka.

5.2.3. Merged Data Set

[27] The contributions of the EMs obtained by unmixing the merged data set from GeoB 13602–1 and 13601–4 are similar to the EM models for the separate cores (compare Figures 4d and 4e with

Table 2. IRM Component Analyses of EMs Derived by Unmixing Each Core and the Merged Data Set

	IRM Component 1			IRM Component 2			IRM Component 3			IRM Component 4		
	SIRM	$B_{1/2}$ (mT)	DP	SIRM	$B_{1/2}$ (mT)	DP	SIRM	$B_{1/2}$ (mT)	DP	SIRM	$B_{1/2}$ (mT)	DP
						GeoB 13602-1						
$S1_N$	0.14	17.78	0.29	0.64	32.36	0.25	0.14	199.53	0.35	0.08	1621.81	0.35
$S2_N$	0.2	20.42	0.29	0.50	51.29	0.23	0.15	199.53	0.30	0.20	1584.89	0.35
$S3_N$	0.09	14.13	0.3	0.91	64.57	0.17						
$S4_N$	0.23	39.81	0.38	0.46	154.88	0.13	0.31	323.59	0.25	0.01	1584.89	0.35
						GeoB 13601-4						
$S1_S$	0.05	15.85	0.35	0.74	36.31	0.26	0.12	158.49	0.33	0.14	1584.89	0.33
$S2_S$	0.11	16.22	0.29	0.89	64.57	0.17						
$S3_S$		0.18	39.81		0.48	147.91	0.12	0.34	331.13			
						Merged Dataset						
S1	0.21	17.78	0.3	0.56	30.20	0.2	0.13	199.53	0.31	0.13	1584.89	0.31
S2	0.2	17.78	0.3	0.56	51.29	0.25	0.07	199.53	0.28	0.20	1258.93	0.35
S3	0.065	19.95	0.33	0.94	64.57	0.17						
S4	0.18	39.81	0.35	0.52	112.20	0.23	0.28	263.03	0.25	0.00	1584.89	0.32

Figures 4f and 4g). In the lower interval of the cores, the contribution of ***S3*** is lower than $S3_N$ and $S2_S$ while the contribution of ***S4*** is higher compared to $S4_N$ and $S3_S$ from the individual cores. Above the diagenetically affected zones, all trends and local peaks are depicted. However, the merged model has smoother expressions than in the individual GeoB 13601–4 model because of the extra fourth EM ***S2*** in the merged data set. An exception is a peak in ***S1*** during HS 4, which was not expressed in the individual EM models. According to our starting hypothesis, that fluvial sediments are only to be expected at the northern site, the marginal contribution of ***S2*** in GeoB 13601–4 supports such a scenario. The high abundance of ***S1*** during HSs, which correspond to phases of dry conditions on the continent and high dust export [*Mulitza et al.*, 2008, *Itambi et al.*, 2009] suggest that ***S1*** corresponds to an aeolian EM. This outcome of the EM analysis illustrates that our approach is well suited to unmix the terrigenous fractions.

5.3. Magnetic Mineralogy of Rock Magnetic End-Members

[28] We aim to further elucidate the nature of all EMs through more quantitative analysis of the magnetic mineralogy. The EM model of the merged data set largely matches and supports the findings of the two core-specific EM analyses; therefore, we focus on the pooled EM system.

5.3.1. IRM Component Analysis

[29] IRM components for the separate EMs are listed in Table 2. Figure 5 visualizes the fit for the EMs of the merged data set. The shape of the IRM acquisition curve indicates that ***S1*** is a mixture of low-coercivity and high-coercivity magnetic minerals (magnetite and hematite and/or goethite, respectively). Four components (1–4) with increasing magnetic hardness (Figure 5a) are present. Two magnetically soft components ($B_{1/2}$ ~18 mT; $B_{1/2}$ ~30 mT) account for 11% and 68% of the total SIRM, respectively. The soft-magnetic components correspond to magnetite. IRM coercivity spectra of PSD and MD magnetite often depart from lognormal distributions, i.e., they have left-skewed distributions [*Egli*, 2003] due to thermal activation effects [*Egli and Lowrie*, 2002]. The left-skew cannot be fitted with the *Kruiver et al.* [2001] approach and a second associated component is required to properly fit components to the data to account for the skewness. We suggest that component 1 is attributed to this skewness and does not represent an additional magnetic phase. Component 3 ($B_{1/2}$ ~260 mT) accounts for 11.5% of SIRM and is interpreted as hematite, while component 4 ($B_{1/2}$ ~1660 mT) contributes only 8% to the total SIRM and is interpreted as goethite.

[30] The IRM acquisition curve for ***S2*** (cf. Figures 4h and 4i) is relatively similar to that of ***S1***. However, acquisition starts at slightly higher fields (20 mT) and its initial slope is less steep and rises linearly (on a logarithmic scale) at higher fields with a somewhat steeper gradient. The proportion of magnetically soft (magnetite) phases relative to the hard hematite and goethite phases is therefore lower for ***S2***. Two soft components ($B_{1/2}$ ~18 mT, $B_{1/2}$ ~50 mT) that carry 11% and 69% of the total SIRM for ***S2*** are identified as magnetite with a left-skewed coercivity

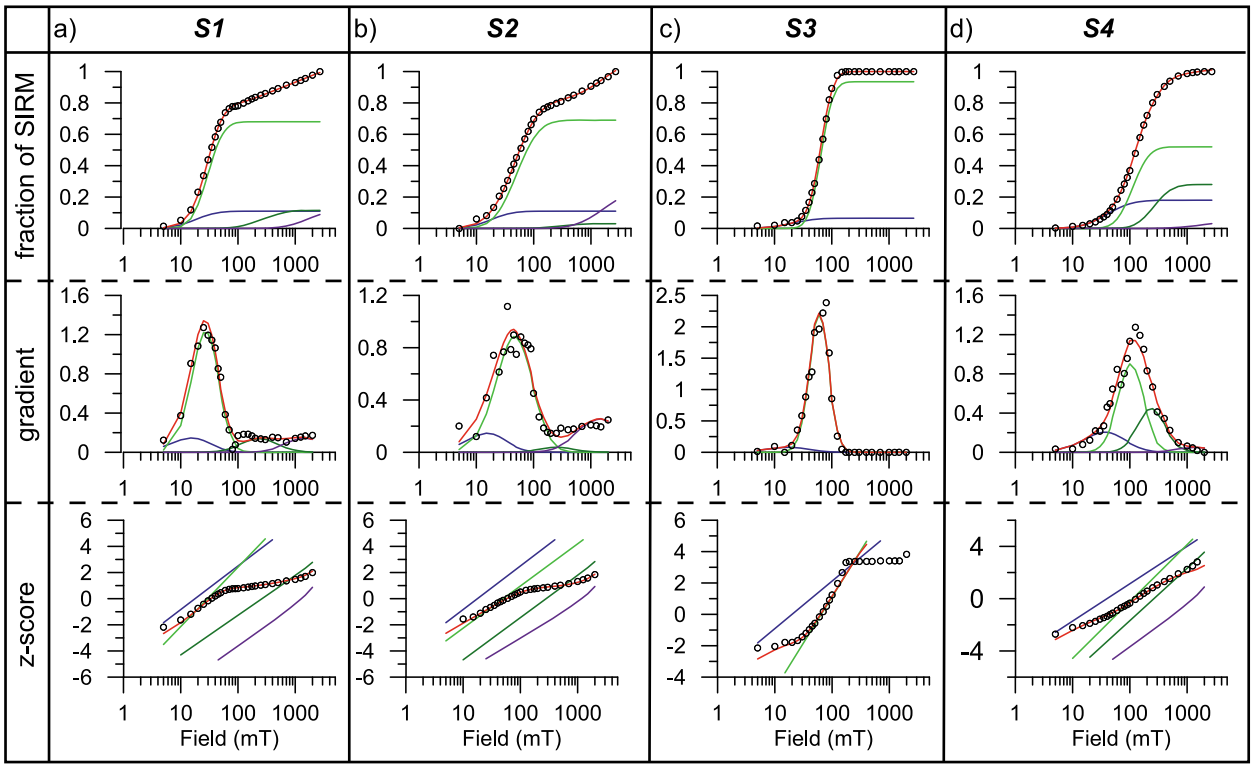

Figure 5. IRM component analyses of EMs (merged data set). Each column corresponds to one EM. Different colors indicate the components needed to fit (red curve) the IRM acquisition curve (black dots). (top row) Linear acquisition plot; (middle row) gradient acquisition plot; and (bottom row) standardized acquisition plot.

spectrum (Figure 5b). Compared to ***S1*** ($B_{1/2}$ ~30 mT), this magnetite is harder and accordingly represents finer grain sizes. Two high-coercivity components ($B_{1/2}$ ~280 mT, $B_{1/2}$ ~1660 mT) contribute to 3% and 25% of the total SIRM and are attributed to hematite and goethite, respectively. The lower hematite to goethite ratio in ***S2*** compared to ***S1*** is striking. Additionally, the higher concentration of a coarse magnetite phase in ***S1*** is in line with the observed physical grain sizes of fluvial [*Gac and Kane*, 1986] and aeolian [*Stuut et al.*, 2005] material from dust- or fluvial-dominated periods off the NW African coast [*Mulitza et al.*, 2008]. These observations support the tentative interpretation of ***S1*** as an aeolian and ***S2*** as a fluvial EM (cf. section 5.2).

[31] ***S3*** (Figure 5c) acquires remanence over a narrow field interval and reaches complete saturation at 120 mT. For a CLG fitting of this EM, two components are needed. Component 1 ($B_{1/2}$ ~20 mT) carries only 6.5% of SIRM, while Component 2 ($B_{1/2}$ ~65 mT) contributes the remaining 93.5%. This fraction is interpreted as bacterial magnetite, which owes its relatively high coercivity to the chain-like arrangement of the fossil SD sized magnetosomes [e.g., *Petersen et al.*, 1986; *von Dobeneck et al.*, 1987; *Vali et al.*, 1989]. Component 2 resembles the 'biogenic hard' component identified by *Egli* [2004b] with a $B_{1/2}$ of 66 mT and DP of 0.11.

[32] Remanence acquisition in ***S4*** takes place mainly at intermediate fields from 0.1 to 1 T, where hard magnetic minerals acquire an IRM. Component 1 ($B_{1/2}$ ~40 mT) carries 18%, component 2 ($B_{1/2}$ ~112 mT) 52%, component 3 ($B_{1/2}$ ~260 mT) 28% and component 4 ($B_{1/2}$ ~1580 mT) accounts for a mere 4% of total SIRM. Component 4 probably represents goethite. Due to its low SIRM, which is up to 200–500 times lower than that of magnetite, the quantity of goethite expressed on a molar or mineralogic basis must be high. Component 3 corresponds to hematite and the relatively hard component 2 most likely represents a relict Ti-rich ferrous hemoilmenite or titanomagnetite phase that survived reductive diagenesis [*Bloemendal et al.*, 1993; *Emiroglu et al.*, 2004; *Nowaczyk*, 2011]. Component 1 may either represent a left skew of component 2, as argued above, or it may consist of alteration-resistant small magnetic inclusions in a silicate matrix [*Hounslow and Maher*, 1996; *Hounslow and Morton*, 2004; *Maher et al.*, 2009]. The latter interpretation is consistent with the rock magnetic record, where ***S4*** is

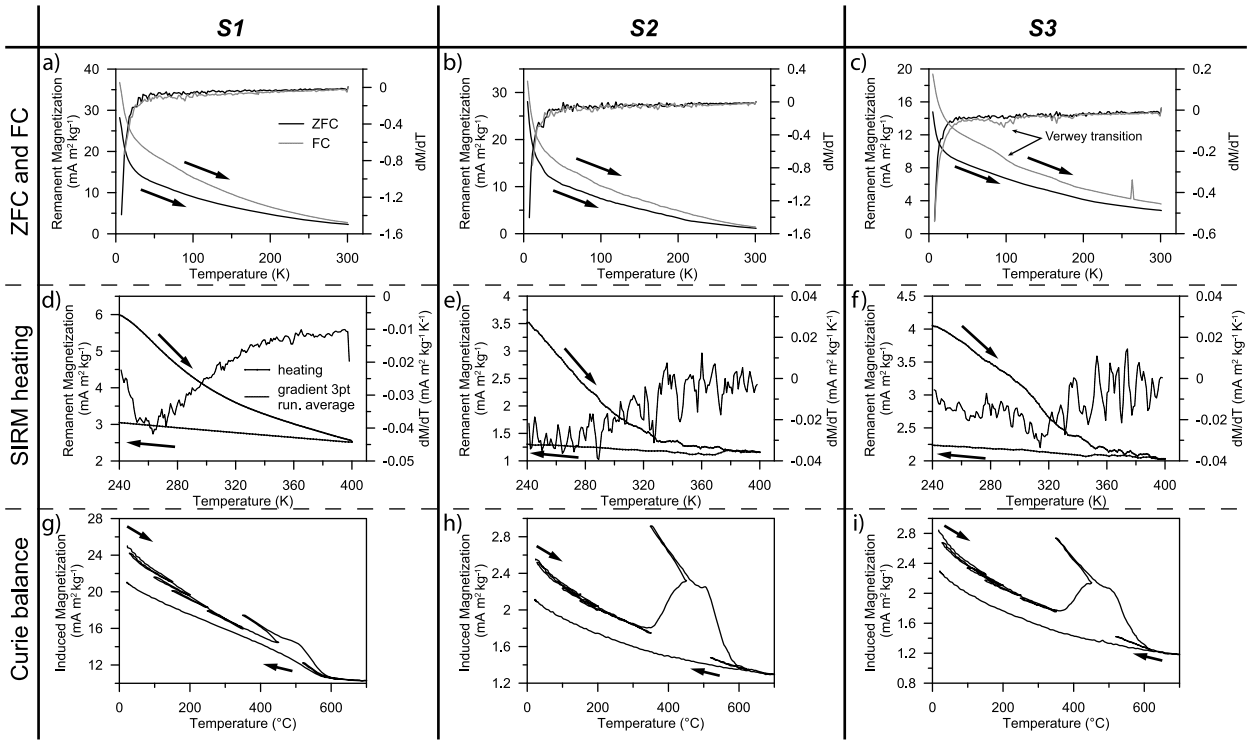

Figure 6. Low- and high-temperature measurements of samples from intervals with dominant end-member contributions of (a, d, g) ***S1***, (b, e, h) ***S2***, and (c, f, i) ***S3***. The notable convergence of ZFC and FC warming curves (Figures 6a–6c) and the marked loss of magnetization while heating to ~350 K (Figures 6d–6f) points to the presence of goethite. The Verwey transition is evident in the data from the sample dominated by ***S3*** (Figure 6c). Curie balance measurements (Figures 6g–6i) indicate a thermal alteration of pyrite to magnetite. The pyrite content appears to be lowest in the ***S1*** sample (Figure 6g).

only prominent in the magnetically depleted lower parts of both cores.

5.4. Additional Rock Magnetic Analyses

[33] To supplement and further support the EM analysis and IRM component interpretation, we performed high- and low-temperature rock magnetic measurements for three samples from GeoB 13602–1 with dominant ***S3*** (8.2 ka), ***S2*** (13.6 ka) and ***S1*** (15.5 ka) contributions, respectively.

5.4.1. Low- and High-Temperature Magnetic Properties

[34] ZFC and FC warming curves for ***S1*** and ***S2*** samples converge with increasing temperature, in particular in the interval 20–100 K (Figures 6a and 6b). This effect is less pronounced in the ***S3*** sample (Figure 6c). The acquisition of remanence during FC and convergence of FC and ZFC curves has been observed for goethite samples [*Liu et al.*, 2006] and has also been attributed to the presence of goethite in pelagic sediments [*Franke et al.*, 2007]. *Smirnov and Tarduno* [2000] recognized a similar convergence in samples from the equatorial Pacific Ocean but did not find any evidence for the presence of goethite. Our SIRM heating experiments indicate a dramatic loss in magnetization while heating up to ~330 K (Figures 6d–6f). Notably, this temperature is lower than the blocking temperatures for pure goethite, however, due to isomorphous Al-substitution, which is typical for pedogenically formed goethites [*Fitzpatrick and Schwertmann*, 1982], and excess water in the structure, lower blocking temperatures are often observed [*Lowrie and Heller*, 1982; *Dekkers*, 1989; *Liu et al.*, 2006]. We thus attribute both the convergence of ZFC and FC curves and the SIRM loss to the presence of goethite which is also detected by the IRM component analyses. Although the ***S3*** end-member has the lowest contribution of goethite (compare Table 2), the SIRM heating experiment reveals a significant amount of goethite for the ***S3*** sample. When taking the ratio of SIRM before and after heating (rSIRM) as an indicator of the proportion of SIRM contributed by goethite with respect to hematite and magnetite, we find rSIRMs

of 1, 1.8 and 0.8 for ***S1***, ***S2*** and ***S3***, respectively. This trend is in accordance with the results of the IRM component analyses. However, the still significant proportion of goethite most probably results from the higher field that was applied for the heating experiment (7 T) while the maximum field was 2.7 T for the IRM acquisition. Hence, very hard magnetic mineral phases acquired remanence. Second, it has to be noted that the ***S3*** sample corresponds to a mixture of 24% ***S1***, 9% ***S2*** and 67% ***S3***. This means that also the goethite from ***S1*** and ***S2*** are visible in the thermomagnetic measurements of the "***S3***" sample.

[35] In contrast with the two other samples, the FC curve of the ***S3*** sample (Figure 6c) has a Verwey transition that is indicative of stoichiometric SD magnetite as produced by magnetotactic bacteria [*Moskowitz et al.*, 1993]. Further evidence arises from the analyses of first-order-reversal curves (supplementary Figure S1). The absence of the Verwey transition in the ***S2*** and ***S1*** samples hints at oxidation [e.g., *Özdemir et al.*, 1993] or Ti-substituted magnetites [e.g., *Kakol et al.*, 1992]. The Curie balance cycles (Figures 6g–6i) indicate a strong increase in induced magnetization during heating within a temperature interval of 350–450°C which has been attributed to oxidation of framboidal pyrite [*Passier et al.*, 2001]. This effect and thus the concentration of pyrite is lowest in the ***S1*** sample.

5.4.2. Electron Microscopy

[36] In the heavy liquid separates, magnetic particles appear to be sparse compared to the high amounts of paramagnetic Ti oxides. On the other hand, pyrite is found frequently in all heavy liquid extracts. Framboidal pyrite is abundant in microenvironments like foraminifera tests (Figure 7a) [e.g., *Roberts and Turner*, 1993; *Rowan et al.*, 2009]. In the magnetic extracts, Fe-Ti oxides can reach diameters of up to 40 μm (Figures 7c and 7d). The physical grain size mode of present-day dust collected offshore of Africa is mostly 8–42 μm but can reach grain sizes of 200 μm [*Stuut et al.*, 2005]. Therefore, these coarse-grained Fe-Ti oxides were most likely transported by wind. Most of those grains have subregular morphologies, which might be attributed to mechanical abrasion and/or fragmentation during transport (Figures 7b, 7d, and 7e). However, some grains are idiomorphic (Figure 7f). The EDS analyses reveal varying Fe:Ti ratios between 1:2 and 3:1. Nearly pure magnetite grains also occur. Ti-Fe oxides have shrinkage cracks (Figure 7d), which indicate low-temperature oxidation [*Petersen and Vali*, 1987]. Ilmenite exsolution lamellae, which are typical for Ti-rich titanomagnetite, are preserved as skeletons in some grains (Figure 7d) while the more unstable magnetite has been dissolved under reducing conditions [*Canfield et al.*, 1992; *Nowaczyk*, 2011]. *Gehring et al.* [1997, 2007] and *Fischer et al.* [2008] inferred from magnetite dissolution in soil samples from Mali that the prevailing strong seasonality induces fluctuating redox conditions in the soils. Since pyrite is very sparse in the representative ***S1*** sample (cf. Figure 6g) we suggest that dissolution had already occurred during pedogenesis in the source area.

[37] TEM analyses reveal that the sub-micron magnetic fraction has a high abundance of fossil magnetosomes (Figures 8a, 8b, 8c, and 8f) with cuboctahedral or bullet-shaped morphologies organized in long chains or clusters (Figures 8b and 8c). Electron diffraction patterns indicate that the magnetosomes consist of magnetite (Figures 8d and 8e). To estimate and compare their concentration in the three studied samples is difficult. However, the 'aeolian' ***S1*** sample (Figure 8g) has by far the lowest amount of magnetosomes with respect to detrital particles which consists mainly of titanomagnetites and silicates. The presence of silicates in magnetic extracts points to magnetite inclusions within the host grains as pointed to in Figure 8g. In the submicron fraction of the ***S3*** sample only magnetosomes were identified.

6. Discussion

[38] The magnetic mineral inventory of the aeolian and fluvial EMs can be used to assess the paleoenvironmental conditions in the source areas. The pedogenic signature of magnetic iron oxides in terrestrial soils [*Kämpf and Schwertmann*, 1983; *Schwertmann and Taylor*, 1989; *France and Oldfield*, 2000] and loess sequences [*Maher*, 1986; *Maher and Thompson*, 1992; *Spassov et al.*, 2003] has been widely studied. Parent rock petrology, Eh/pH conditions and water content control the speciation of pedogenic iron minerals [*Kämpf and Schwertmann*, 1983]. As the ratio of pedogenic hematite/goethite lowers with decreasing soil temperature and excess moisture [*Maher*, 1986; *Schwertmann and Taylor*, 1989], the ratio of these minerals can be related to climatic variations. Accordingly, in the South China Sea [*Zhang et al.*, 2007], and off the Amazon [*Harris and Mix*, 1999], the hematite and goethite concentrations

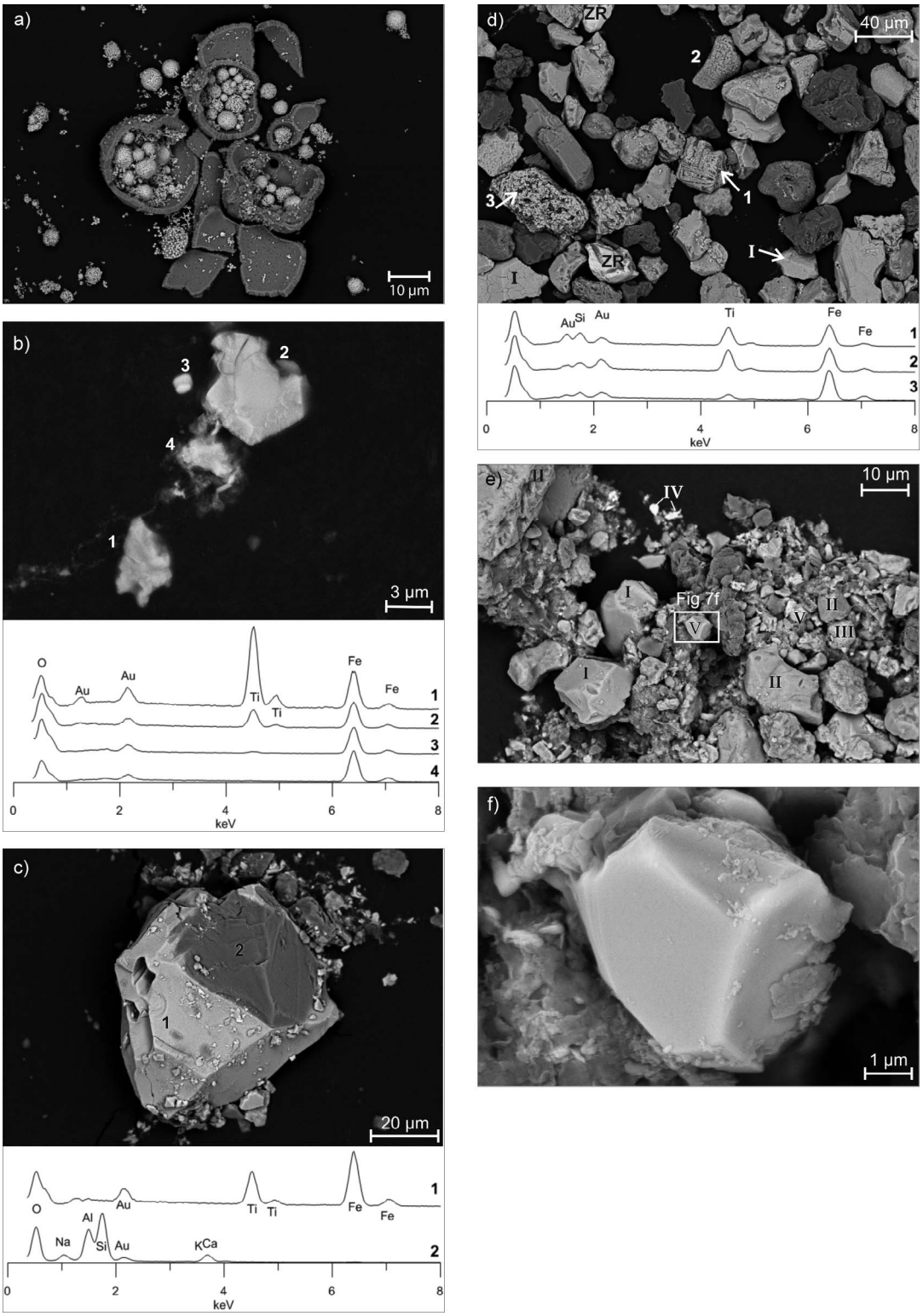

Figure 7. SEM photographs and elemental spectra for grains obtained after heavy liquid (Figure 7a) and magnetic extraction (Figures 7b–7f). (a) Pyrite precipitated in foraminifera tests (heavy liquid separate). (b) Ti-Fe oxides with varying Ti/Fe ratios; analyses correspond to numbered grains. (c) Rock fragment of magnetite and silicate (feldspar) rim. (d, e) Ti-Fe oxides with varying Fe/Ti ratios: I: 1:1, II: 1:2, III: 3:1, V: nearly pure magnetite, IV: chromite, ZR: zircon. Some grains have shrinkage cracks (Figure 7d, lower left and right of the picture) and skeletal ilmenite lamellae (1). (f) Close-up of idiomorphic magnetite grain.

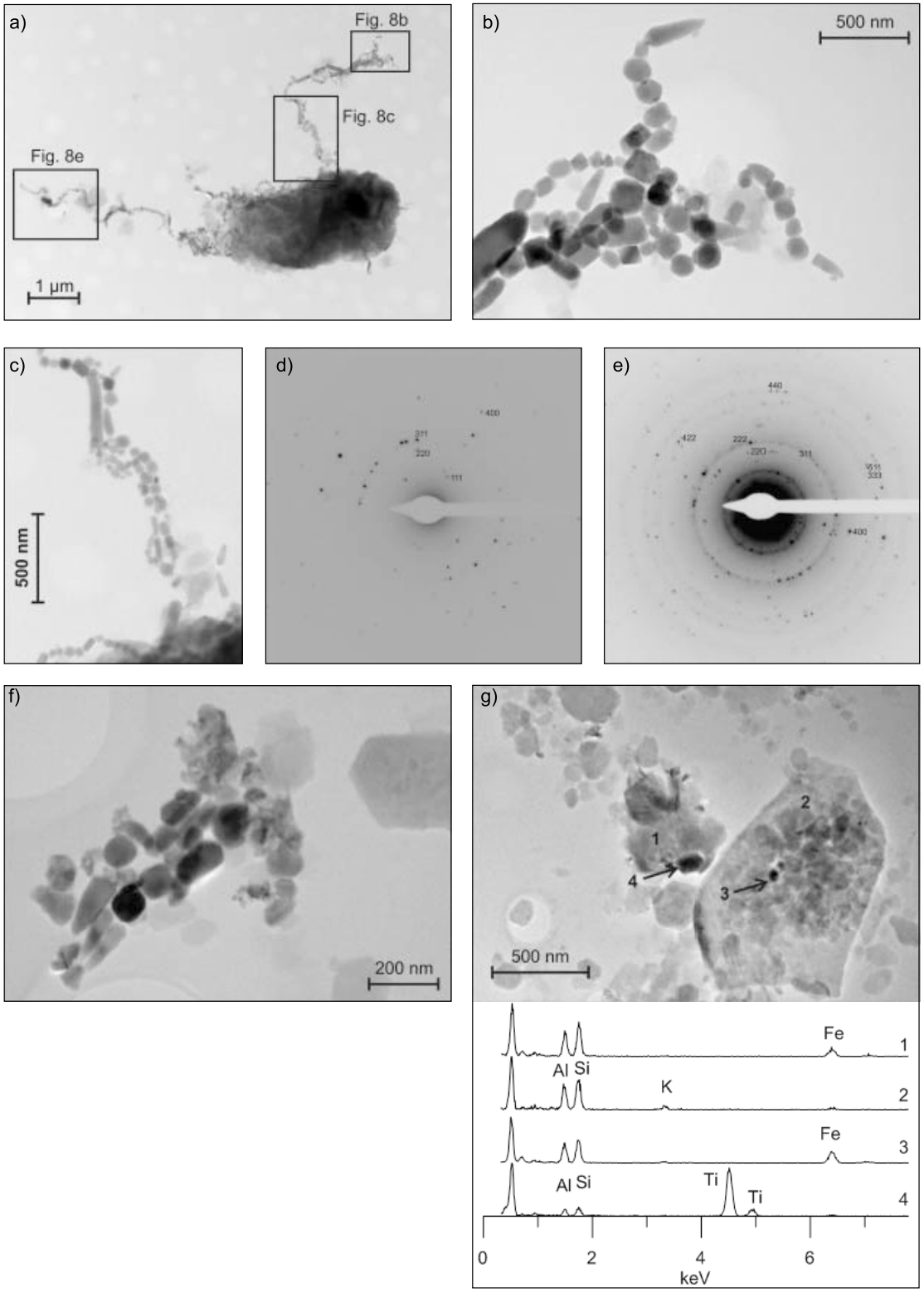

Figure 8. TEM photographs and diffraction patterns. Sample dominated by ***S3***: (a) siliceous mineral surrounded by bacterial magnetite chains. (b, c) Close-ups of bacterial chains with mainly cubo-octahedral and bullet-shaped magnetosomes. (d) Diffraction pattern of Figure 8a and (e) the area of the lower left chain. (f) Cluster of cubo-octahedral and bullet-shaped grains (***S2*** sample). (g) ***S1*** sample that contains the lowest concentration of magnetosomes, but with many siliceous grains (spectra 1, 2) and detrital Fe-Ti oxides (3, 4) in the sub-micron fraction.

have been used to reconstruct past precipitation. However, this ratio must be handled carefully. In settings where reductive diagenesis occurs, an increase of this ratio could simply result from goethite dissolution with respect to the more stable hematite [*Abrajevitch et al.*, 2009; *Abrajevitch and Kodama*, 2011].

6.1. Aeolian Signature

[39] The high hematite/goethite ratio of ***S1*** suggests that relatively dry conditions prevailed during terrestrial pedogenesis. *Sarnthein et al.* [1981] and *Bloemendal et al.* [1988, 1992] found that dust derived from the southern Sahara and northern Sahel contains a high hematite content, mainly as coatings on quartz grains. Similar results have recently been found for terrestrial sand samples from these regions. It is inferred that these hematite coatings are secondary minerals that formed within soils [*Lyons et al.*, 2010]. A high frequency dependence of susceptibility in the HS 1 interval in GeoB 13602–1 (cf. Figure 3a), where ***S1*** is dominant underlines the presence of a SP phase associated with this fraction.

6.2. Fluvial Signature

[40] Soils and desert sand samples from the Sahara and Sahel contain abundant high coercivity minerals in areas with higher precipitation [*Lyons et al.*, 2010]. However, *Lyons et al.* [2010] did not discriminate between hematite and goethite in the subtropical soil samples.

[41] Under more humid conditions in the catchment area of the Gambia River, pedogenic goethite should be more abundant than hematite [*Maher*, 1986; *Schwertmann and Taylor*, 1989]. Lush savanna vegetation must have prevented soil mobilization by wind while sheet and stream erosion in rainy seasons were favored. Based on XRD analyses *Gac and Kane* [1986] reported that bulk fluvial sediments from the Senegal River, which drains a larger, but climatically similar basin as the Gambia River, also contain goethite.

[42] Our interpretation of ***S2***, which is only dominant in proximal core GeoB 13602–1, as having a fluvial origin is supported by satellite images showing that the Gambia fresh water plume is presently deflected to the north. Our data indicate that during MIS 1–3 northward-directed surface currents prevailed so that the fluvial material was equally deposited at the northern site. Coercivity and thermomagnetic analyses from peak concentration samples suggest relatively low concentrations of magnetite and hematite and a particularly high concentration of goethite. ***S2*** levels are particularly high during the early AHP.

6.3. Bacterial Signature

[43] ***S3*** represents a magnetic mineralogy with a narrow coercivity spectrum. Coercivity spectra with such low dispersions have only been observed for magnetite or greigite formed within the cells of magnetotactic bacteria [*Kruiver and Passier*, 2001; *Egli*, 2004a; *Vasiliev et al.*, 2007]. However, high temperature magnetic measurements rule out the presence of greigite because the typical irreversible break-down of greigite between 200 and 400°C [*Reynolds et al.*, 1994; *Vasiliev et al.*, 2007] is not detectable. TEM analysis unequivocally reveals that magnetosomes are present and extremely abundant in the interval where ***S3*** dominates. Previously, a hard magnetite phase in core material off the Gambia and Senegal Rivers was linked to fluvial sediments [*Itambi et al.*, 2010]. Magnetosomes were considered unlikely to be a significant contributor to the sediment magnetic properties in the environment offshore of NW Africa for two main reasons. First, in areas with high terrigenous input and high concentration of magnetic minerals, the magnetic signature of magnetosomes would be insignificant compared to that of the terrigenous signal. Second, magnetotactic bacteria occur above the iron-redox boundary [*Karlin et al.*, 1987; *Petermann and Bleil*, 1993] and magnetite magnetosomes should rapidly dissolve during burial with upward migrating iron-redox boundary [e.g., *Hilgenfeldt*, 2000]. However, our results indicate that magnetosomes contribute up to 60% of the SIRM and are preserved even between the present iron-redox boundary and the sulfidic zone (cf. section 6.4). The coercivity distribution of the bacterial magnetite phase is similar to the bacterial 'hard' component identified of *Egli* [2004a], which was inferred to be more resistant toward anoxic conditions. The presence, though low contribution, of ***S3*** in the lower intervals of the records, is unlikely to be linked to fossil magnetosomes that survived reductive dissolution. We infer that here the contribution of ***S3*** is more likely attributed to SD magnetite inclusions [*Hounslow and Maher*, 1996; *Hounslow and Morton*, 2004].

[44] The downcore record of GeoB 13602–1 reveals that the contribution of the bacterial EM $\boldsymbol{S3_N}$ (Figure 4) is somehow correlated to the carbonate content, and organic carbon (cf. Figure 2b). It appears that in the upper part of the core, increases and decreases in the ***S3*** contribution lag the carbonate record by ~0.2 m. In pelagic sediments the

availability of nutrients [*Hesse*, 1994], e.g., iron [*Roberts et al.*, 2011a] is an important factor for the occurrence of magnetotactic bacteria, while the input of organic matter and linked oxygenation states of the subsurface have to be balanced for a colonization and preservation in the geological record [*Roberts et al.*, 2011a]. *Lean and McCave* [1998] suggested that decrease in carbon flux and thus a thickening of the aerobic zone during interglacials, would have left a longer time for the colonization of magnetotactic bacteria, while in other settings their abundance is positively linked to organic carbon input [*Roberts et al.*, 2011a]. We compared the ***S3*** contribution and organic carbon concentration on a terrigenous-free basis, i.e., normalized to the proportion of carbonate (data not shown) and found that variations of ***S3*** contributions are mainly controlled by dilution of terrigenous sediments.

6.4. Diagenetic Signature

[45] The prominent change in magnetic properties in the lower sections and the near-surface layer of the cores reflects a near-complete loss of fine-grained Fe oxide mineral particles. Reductive dissolution of iron oxides is a function of surface area [*Canfield and Berner*, 1987], therefore fine-grained magnetite is more rapidly and pervasively dissolved [*Karlin and Levi*, 1983]. In zones where ***S4*** dominates, SIRM is extremely low. The relict magnetic mineral inventory consists of intermediate- and high-coercivity minerals and probably correspond to Ti^{4+}-rich and therefore Fe^{3+}-poor Fe-Ti oxide phases as well as some apparently more resistive antiferromagnetic mineral phases [*Robinson et al.*, 2000; *Emiroglu et al.*, 2004; *Garming et al.*, 2005; *Dillon and Bleil*, 2006; *Nowaczyk*, 2011].

[46] We suggest that the lower diagenetically depleted zone should have sulfidic conditions. Although no pore water data are available, we suspect that the sharp transition marks the modern sulfate-methane transition (SMT). Above, iron oxides are reduced to pyrite only in organic rich microenvironments like foraminifera tests [*Mohamed et al.*, 2011]. The magnetite loss in the narrow subsurface horizon could result from (most likely microbially mediated) redox reactions at the present iron-redox boundary [*Tarduno and Wilkison*, 1996; *Riedinger et al.*, 2005]. Under steady state redox conditions, the iron-redox boundary would have migrated successively upward in equilibrium with sedimentation and would have led to dissolution of fine-grained iron (oxyhydr)oxides. However, high bacterial magnetite contents between the modern iron-redox boundary and the present SMTZ rule out such a gradual migration. *Karlin* [1990] reported the preservation of ultra fine-grained magnetite in certain intervals in a core below the present iron-redox boundary. He inferred nonsteady state redox conditions, which he attributed to varying sedimentation rates. Compared to the Holocene, sedimentation rates in GeoB 13602–1 doubled during MIS 2 and MIS 3 and were even up to seven times higher during HS 1 and the Younger Dryas (cf. Figure 2). We therefore infer that the enhanced sedimentation rates during the MIS 3 and MIS 2 led to rapid burial of detrital and authigenic iron-oxides (magnetosomes) and to a rapid upward migration of the iron redox boundary, and accordingly, the preservation of the biogenic magnetic minerals.

[47] The near-surface depleted layer is located just below an organic carbon peak (and associated carbonate minimum) in the uppermost 10 cm of GeoB 13602–1 (Figure 2), which dates to the termination of the AHP at 5.5 ka [*deMenocal et al.*, 2000]. Variations in the organic carbon supply could also influence the more pervasive dissolution of magnetic minerals in this near-surface zone [e.g., *Tarduno and Wilkison*, 1996]. Over the rest of the Holocene and LGM organic carbon contents are much lower, especially during HS 1, probably because of lower productivity and higher dilution of organic matter by siliciclastics.

[48] Magnetite depletion in both, deep and in subsurface sediment layers is also evident in nearby cores (cf. Figure 1a) GeoB 9527–5 (close to GeoB 13601–4) and GeoB 9506–1 from the continental margin in the Sahel, but is absent in core GeoB 9516–5 [*Itambi et al.*, 2009] which is close to GeoB 13602–1. The ages attributed to the reductive layers are different for the cores investigated by *Itambi et al.* [2009] and those from our study. However, the sedimentation rates in those cores are half as high as in ours, which will have a significant impact on the organic carbon content, pore water geochemistry, and reductive diagenesis [e.g., *Tarduno and Wilkison*, 1996].

6.5. Paleoclimatic Implications

[49] Unmixing of the terrigenous fraction enables an estimation of dust/river variations in our record. Distinction of dust emitted from different source areas is not evident from our data. We therefore cannot infer whether dust was transported by the Trades or AEJ. This suggests that dust either originates from only one source area, or that the EM unmixing of IRM acquisition curves is not capable of differentiating between different dust sources. The latter could be due to

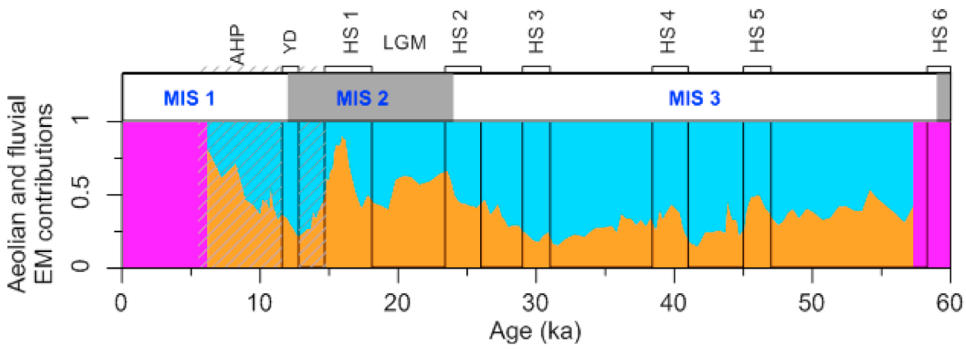

Figure 9. Down-core record (0–60 ka) of ***S1*** (orange) and ***S2*** (blue) for core GeoB 13602–1 normalized to their cumulative values derived from the merged data set (cf. Figure 4f). During HS 5, HS 4, the LGM and HS 1 dust input is enhanced. During the AHP, conditions are comparable to MIS 3. The interval within which the SIRM is strongly reduced, and where reductive diagenesis has affected the record (also expressed by a strong contribution of ***S4***), is colored pink.

(a) a similar magnetic mineralogy of soils in the source areas, (b) a co-variation of AEJ and Trades input or (c) covariation of an undistinguished dust fraction and river supply.

[50] Changing proportions of fluvial and aeolian EMs reflect environmental and paleoclimatic changes in the study area. Figure 9 shows contributions of ***S1*** and ***S2*** normalized to 1, i.e., without the varying contribution of bacterial magnetite. The intervals of reductive diagenesis are not considered. We only show the plot for GeoB 13602–1 because ***S2*** is virtually absent in GeoB 13601–4. Peaks in ***S1*** during HS 5, HS 4, LGM and HS 1 indicate (much) drier conditions during those periods. In contrast, our data do not indicate dry conditions during HS 3.

[51] Contemporaneous to the deposition of Heinrich Layers (HL) in the North Atlantic, 'dusty events' [*Jullien et al.*, 2007] are noticed in sediment records of low latitudes. These were associated with reduced meridional overturning and a southward shift of the ITZC and the associated rain belt [*Mulitza et al.*, 2008]. In the North Atlantic, the geochemical signature of the detritus in HL 1, HL 2, HL 4, and HL 5 suggests Canadian sources [e.g., *Hemming et al.*, 1998], while HL 3 sediments were probably derived from Greenland and Scandinavia [*Gwiazda et al.*, 1996]. Numerical models by *Seidov and Maslin* [1999] on the influence of meltwater injections into the North Atlantic indicate that not the total amount of meltwater but its ingression to the convection site is most effective in disturbing NADW production. It was suggested that deep water formation resumed more rapidly at the end of Heinrich event 3 with respect to the stronger Heinrich events 1, 2, 4, 5 [*Elliot et al.*, 2002]. It may further be hypothesized that less arid conditions are a low-latitude expression of a weaker disturbance of the meridional overturning circulation.

[52] By far the highest contribution of dust occurs during HS 1. Similar results have been suggested from rock magnetic records [*Itambi et al.*, 2009] and from geochemical proxies [*Mulitza et al.*, 2008]. This indicates that the ITZC (and rain-belt) retreated further to the south during HS 1 with respect to all remaining HSs. The ITCZ shift also induces a longer season of prevailing NE Trades. We additionally infer that the longer duration of arid conditions during the LGM and associated reduced vegetation cover in the hinterland [e.g., *Mahowald et al.*, 1999] exposed larger areas for aeolian deflation. The combination of aridity and stronger or longer Trade winds season are probably responsible for the high dust content during HS 1. Studies of past dust accumulation off NW Africa have been integrated in the DIRTMAP Project [*Kohfeld and Harrison*, 2001], of which the sites in the proximity of our study region have 2 to 6 times higher dust accumulation during the LGM compared to the present.

[53] Fluvial EM ***S2*** is literally absent during HS 1, therefore the terrigenous fraction (cf. Figure 2) corresponds exclusively to dust. Since terrigenous sedimentation rate during HS 1 is much higher with respect to the other HSs and the LGM (see Figure 2), we infer that dust export from the NW African continent was at least twofold higher with respect to the remaining HSs and even four times higher with respect to the LGM.

[54] Recently, *Roberts et al.* [2011b] found that dust export from the Arabian-Chinese dust belt was much stronger during glacial terminations and, accordingly, accompanying HSs than during glacial

maxima. These periods have been linked to less precipitation in the Eurasian deserts due to a weaker monsoon [*Roberts et al.*, 2011b]. Their findings in conjunction with similar arid conditions in NW Africa underline the teleconnection between the North Atlantic and northern hemisphere atmosphere dynamics.

[55] After HS 1, ***S2*** gains more influence indicating more humid conditions. This period corresponds to the early AHP [*Ritchie et al.*, 1985; *deMenocal et al.*, 2000], while during the late AHP the fluvial influence decreases. A return to more arid conditions during the Younger Dryas, which has been reported from gravity cores off the Senegal River [*Mulitza et al.*, 2008] is not evident in our core. However, their study site lies about 400 km north of our study area and desertification and associated dust export did possibly not retreat as far south during the Younger Dryas. Similar conclusions have been drawn from geochemical proxies [*Collins et al.*, 2011]. They observed that contrasts of dry conditions during HS 1 and the LGM and humid conditions during the Holocene are strongest off the Sahara desert and diminish toward subtropical Africa.

6.6. Advantages of Environmental Magnetic Methods

[56] As previously published geochemical and grain size studies, our rock magnetic approach is equally capable of detecting changes in fluvial and aeolian contents in marine sediments. From a technical viewpoint magnetic analyses are possibly less time consuming because no sample preparation is needed and measurements can be highly automated. Magnetic minerals are also more resistant to oxic chemical weathering than siliciclastic minerals such as feldspars, and are only subject to mechanical abrasion during transport. Geochemical data of Saharan dust indicate that sediments from the same source area may have differing elemental ratios due to gravitational fractionation during transport [e.g., *Caquineau et al.*, 1998], which is attributed to fall out of coarser components (e.g., quartz and feldspars) with respect to fine (clay) minerals. Accordingly, elemental ratios as well as grain size distributions of aeolian and fluvial material may be influenced by differing transport energies (e.g., higher wind speeds or energetically higher river discharge). Similar to approaches using clay minerals [*Caquineau et al.*, 1998, 2002], even in combination with grain size data and elemental ratios [*Stuut et al.*, 2005], magnetic mineralogy is helpful for explicitly identifying sediments from different source areas. Moreover, since the formation of pedogenic iron-oxides is highly dependent on environmental settings, information about climatic conditions in the source areas may be inferred. However, our study shows that when using magnetic properties for paleoclimatic reconstruction, special attention must be paid to the potential occurrence of magnetotactic bacteria and their contribution to the magnetic signal [*Roberts et al.*, 2011a] even in settings with high organic carbon accumulation and terrigenous input.

7. Conclusions

[57] End-member and IRM component analyses of rock magnetic properties from two contrasting sites enabled us to differentiate magnetic signatures and to quantify contributions of primary, terrigenous source materials and of secondary, post-depositional bacterial biomineralization and diagenetic relict phases to the magnetic mineral assemblage. The main contributors of the terrigenous sediment fraction at the studied sites are dust exported by the African wind systems (NE Trades, African Easterly Jet) and fluvial sediment discharge mainly by the Gambia River. Both terrigenous EMs have marked differences in terms of magnetic mineralogy: Dust contains a higher proportion of magnetite and a lower proportion of goethite/hematite with respect to the fluvial material This feature mirrors the environmental conditions on land because in more humid areas goethite forms in preference to hematite and vice versa. The EM solutions imply drier conditions during the LGM and HSs, especially HS 1, and humidification during the AHP.

[58] Reductive magnetic mineral diagenesis was observed in distinct layers from both cores, a partial depletion in a shallow horizon at a depth of 0.1 to 0.2 m and pervasive depletion below ~7.50 m. These alteration zones seem to mark the modern iron-redox boundary and the sulfate-methane transition zone, respectively. The EM signature of the magnetic relict fraction suggests a relative enrichment of reduction resistant intermediate coercivity minerals such as Ti-rich titanomagnetites and hemoilmenites.

[59] Unexpectedly for settings with high terrigenous inputs, we found high proportions of submicron bacterial magnetite that accounts for up to 60% of total SIRM. This demonstrates the eminent potential contribution of bacterial biomineralization, even in terrigenous marine sediments and complicates the interpretation of magnetic mineral data in terms of sediment provenance. One possibility is to identify such a bacterial EM and subtract its influence to

enable more meaningful analyses of the lithogenic magnetic mineral fraction.

Acknowledgments

[60] We thank the crew and scientific party of *Maria S. Merian* cruise MSM 11/2 for helping to collect the studied cores, Thomas Frederichs for help with MPMS measurements and interpretation, Tom Mullender for helping with Curie balance measurements, Monika Segl for providing oxygen isotope measurements, Hella Buschhoff for carbon content analyses and Petra Witte for driving the SEM. We also thank Andrew Roberts for helpful comments and constructive suggestions from Ramon Egli and one anonymous reviewer. This study was enabled by funded by the Deutsche Forschungsgemeinschaft (DFG) through the international graduate college EUROPROX- Proxies in Earth History and through DFG-Research Center / Cluster of Excellence "The Ocean in the Earth System" MARUM – Center for Marine Environmental Sciences. The data of this study are available in the PANGAE database http://doi.pangaea.de/10.1594/PANGAEA.788162.

References

Abrajevitch, A., and K. Kodama (2011), Diagenetic sensitivity of paleoenvironmental proxies: A rock magnetic study of Australian continental margin sediments, *Geochem. Geophys. Geosyst.*, *12*, Q05Z24, doi:10.1029/2010GC003481.

Abrajevitch, A., R. V. der Voo, and D. K. Rea (2009), Variations in relative abundances of goethite and hematite in Bengal Fan sediments: Climatic vs. diagenetic signals, *Mar. Geol.*, *267*, 191–206, doi:10.1016/j.margeo.2009.10.010.

Bloemendal, J., B. Lamb, and J. King (1988), Paleoenvironmental implications of rock-magnetic properties of late Quarternary sediment cores from the eastern equatorial Atlantic, *Paleoceanography*, *3*, 61–87, doi:10.1029/PA003i001p00061.

Bloemendal, J., J. W. King, F. R. Hall, and S. J. Doh (1992), Rock Magnetism of Late Neogene and Pleistocene deep-sea sediments: Relationship to sediment source, diagenetic processes, and sediment lithology, *J. Geophys. Res.*, *97*, 4361–4375, doi:10.1029/91JB03068.

Bloemendal, J., J. W. King, A. Hunt, P. B. Demenocal, and A. Hayashida (1993), Origin of the sedimentary magnetic record at Ocean Drilling Program sites on the Owen Ridge, western Arabian Sea, *J. Geophys. Res.*, *98*, 4199–4219, doi:10.1029/92JB02914.

Broecker, W. S. (1998), Paleocean circulation during the last deglaciation: A bipolar seesaw?, *Paleoceanography*, *13*, 119–121, doi:10.1029/97PA03707.

Canfield, D. E., and R. A. Berner (1987), Dissolution and pyritization of magnetite in anoxic marine sediments, *Geochim. Cosmochim. Acta*, *51*, 645–659, doi:10.1016/0016-7037(87)90076-7.

Canfield, D. E., R. Raiswell, and S. H. Bottrell (1992), The reactivity of sedimentary iron minerals toward sulfide, *Am. J. Sci.*, *292*, 659–683, doi:10.2475/ajs.292.9.659.

Caquineau, S., A. Gaudichet, L. Gomes, M.-C. Magonthier, and B. Chatenet (1998), Saharan dust: Clay ratio as a relevant tracer to assess the origin of soil derived aerosols, *Geophys. Res. Lett.*, *25*, 983–986, doi:10.1029/98GL00569.

Caquineau, S., A. Gaudichet, L. Gomes, and M. Legrand (2002), Mineralogy of Saharan dust transported over northwestern tropical Atlantic Ocean in relation to source regions, *J. Geophys. Res.*, *107*(D15), 4251, doi:10.1029/2000JD000247.

Chiapello, I., G. Bergametti, L. Gomes, B. Chatenet, F. Dulac, J. Pimenta, and E. S. Suares (1995), An additional low layer transport of Sahelian and Saharan dust over the northeastern Tropical Atlantic, *Geophys. Res. Lett.*, *22*, 3191–3194, doi:10.1029/95GL03313.

Collins, J. A., et al. (2011), Interhemispheric symmetry of the tropical African rainbelt over the past 23,000 years, *Nat. Geosci.*, *4*, 42–45, doi:10.1038/ngeo1039.

Dearing, J. A., R. J. L. Dann, K. Hay, J. A. Lees, P. J. Loveland, B. A. Maher, and K. O'Grady (1996), Frequency-dependent susceptibility measurements of environmental materials, *Geophys. J. Int.*, *124*, 228–240, doi:10.1111/j.1365-246X.1996.tb06366.x.

Dekkers, M. J. (1989), Magnetic properties of natural Goethite II. TRM behaviour during thermal and alternating field demagnetization and low-temperature treatment, *Geophys. J. Int.*, *97*, 341–355, doi:10.1111/j.1365-246X.1989.tb00505.x.

deMenocal, P., J. Ortiz, T. Guilderson, J. Adkins, M. Sarnthein, L. Baker, and M. Yarusinsky (2000), Abrupt onset and termination of the African Humid Period: Rapid climate responses to gradual insolation forcing, *Quat. Sci. Rev.*, *19*, 347–361, doi:10.1016/S0277-3791(99)00081-5.

Dillon, M., and U. Bleil (2006), Rock magnetic signatures in diagenetically altered sediments from the Niger deep-sea fan, *J. Geophys. Res.*, *111*, B03105, doi:10.1029/2004JB003540.

Egli, R. (2003), Analysis of the field dependence of remanent magnetization curves, *J. Geophys. Res.*, *108*(B2), 2081, doi:10.1029/2002JB002023.

Egli, R. (2004a), Characterization of individual rock magnetic components by analysis of remanence curves, 1. Unmixing natural sediments, *Stud. Geophys. Geod.*, *48*, 391–446, doi:10.1023/B:SGEG.0000020839.45304.6d.

Egli, R. (2004b), Characterization of individual rock magnetic components by analysis of remanence curves. 3. Bacterial magnetite and natural processes in lakes, *Phys. Chem. Earth, Parts A, B, and C*, *29*, 869–884, doi:10.1016/j.pce.2004.03.010.

Egli, R., and W. Lowrie (2002), Anhysteretic remanent magnetization of fine magnetic particles, *J. Geophys. Res.*, *107*(B10), 2209, doi:10.1029/2001JB000671.

Elliot, M., L. Labeyrie, and J.-C. Duplessy (2002), Changes in North Atlantic deep-water formation associated with the Dansgaard–Oeschger temperature oscillations (60–10 ka), *Quat. Sci. Rev.*, *21*, 1153–1165, doi:10.1016/S0277-3791(01)00137-8.

Emiroglu, S., D. Rey, and N. Petersen (2004), Magnetic properties of sediment in the Ría de Arousa (Spain): Dissolution of iron oxides and formation of iron sulphides, *Phys. and Chem. Earth, Parts A, B, and C*, *29*, 947–959, doi:10.1016/j.pce.2004.03.012.

Eyre, J. (1996), The application of high resolution IRM acquisition to the discrimination of remanence carriers in Chinese loess, *Stud. Geophys. Geod.*, *40*, 234–242, doi:10.1007/BF02300740.

Fischer, H., J. Luster, and A. U. Gehring (2008), Magnetite weathering in a Vertisol with seasonal redox-dynamics, *Geoderma*, *143*, 41–48, doi:10.1016/j.geoderma.2007.10.004.

Fitzpatrick, R. W., and U. Schwertmann (1982), Al-substituted goethite–An indicator of pedogenic and other weathering environments in South Africa, *Geoderma*, *27*, 335–347, doi:10.1016/0016-7061(82)90022-2.

France, D. E., and F. Oldfield (2000), Identifying goethite and hematite from rock magnetic measurements of soils and sediments, *J. Geophys. Res.*, *105*, 2781–2795, doi:10.1029/1999JB900304.

Frank, U., and N. R. Nowaczyk (2008), Mineral magnetic properties of artificial samples systematically mixed from haematite and magnetite, *Geophys. J. Int.*, *175*, 449–461, doi:10.1111/j.1365-246X.2008.03821.x.

Franke, C., T. Frederichs, and M. J. Dekkers (2007), Efficiency of heavy liquid separation to concentrate magnetic particles, *Geophys. J. Int.*, *170*, 1053–1066, doi:10.1111/j.1365-246X.2007.03489.x.

Frederichs, T., U. Bleil, K. Däumler, T. von Dobeneck, and A. Schmidt (1999), The magnetic view on the marine paleoenvironment: Parameters, techniques and potentials of rock magnetic studies as a key to paleoclimatic and paleoceanographic changes, in *Use of Proxies in Paleoceanography: Examples From the South Atlantic*, edited by G. Fischer and G. Wefer, pp. 575–599, Springer, Berlin, doi:10.1007/978-3-642-58646-0_24.

Gac, J. Y., and A. Kane (1986), Le fleuve Sénégal: I Bilan hydrologique et flux continentaux der matières particulaires a l'embouchure, *Sci. Geol. Bull.*, *39*, 99–130.

Garming, J. F. L., U. Bleil, and N. Riedinger (2005), Alteration of magnetic mineralogy at the sulfate-methane transition: Analysis of sediments from the Argentine continental slope, *Phys. Earth Planet. Inter.*, *151*, 290–308, doi:10.1016/j.pepi.2005.04.001.

Gehring, A. U., G. Guggenberger, W. Zech, and J. Luster (1997), Combined magnetic, spectroscopic, and analytical-chemical approach to infer genetic information for a vertisol, *Soil Sci. Soc. Am. J.*, *61*, 78–85, doi:10.2136/sssaj1997.03615995006100010013x.

Gehring, A. U., H. Fischer, E. Schill, J. Granwehr, and J. Luster (2007), The dynamics of magnetic ordering in a natural hemo-ilmenite solid solution, *Geophys. J. Int.*, *169*, 917–925, doi:10.1111/j.1365-246X.2007.03326.x.

Gwiazda, R. H., S. R. Hemming, and W. S. Broecker (1996), Provenance of icebergs during heinrich event 3 and the contrast to their sources during other heinrich episodes, *Paleoceanography*, *11*, 371–378, doi:10.1029/96PA01022.

Harris, S. E., and A. C. Mix (1999), Pleistocene precipitation balance in the Amazon basin recorded in deep sea sediments, *Quat. Res.*, *51*, 14–26, doi:10.1006/qres.1998.2008.

Hemming, S. R., W. S. Broecker, W. D. Sharp, G. C. Bond, R. H. Gwiazda, J. F. McManus, M. Klas, and I. Hajdas (1998), Provenance of Heinrich layers in core V28–82, northeastern Atlantic: 40Ar/39Ar ages of ice-rafted hornblende, Pb isotopes in feldspar grains, and Nd–Sr–Pb isotopes in the fine sediment fraction, *Earth Planet. Sci. Lett.*, *164*, 317–333, doi:10.1016/S0012-821X(98)00224-6.

Heslop, D. (2009), On the statistical analysis of the rock magnetic S-ratio, *Geophys. J. Int.*, *178*, 159–161, doi:10.1111/j.1365-246X.2009.04175.x.

Heslop, D., and M. Dillon (2007), Unmixing magnetic remanence curves without *a priori* knowledge, *Geophys. J. Int.*, *170*, 556–566, doi:10.1111/j.1365-246X.2007.03432.x.

Heslop, D., G. McIntosh, and M. J. Dekkers (2004), Using time- and temperature-dependent Preisach models to investigate the limitations of modelling isothermal remanent magnetization acquisition curves with cumulative log Gaussian functions, *Geophys. J. Int.*, *157*, 55–63, doi:10.1111/j.1365-246X.2004.02155.x.

Heslop, D., T. von Dobeneck, and M. Höcker (2007), Using non-negative matrix factorization in the "unmixing" of diffuse reflectance spectra, *Mar. Geol.*, *241*, 63–78, doi:10.1016/j.margeo.2007.03.004.

Hesse, P. P. (1994), Evidence for bacterial palaeoecological origin of mineral magnetic cycles in oxic and sub-oxic Tasman Sea sediments, *Mar. Geol.*, *117*, 1–17, doi:10.1016/0025-3227(94)90003-5.

Hilgenfeldt, K. (2000), Diagenetic dissolution of biogenic magnetite in surface sediments of the Benguela upwelling system, *Int. J. Earth Sci.*, *88*, 630–640, doi:10.1007/s005310050293.

Hounslow, M. W., and B. A. Maher (1996), Quantitative extraction and analysis of carriers of magnetization in sediments, *Geophys. J. Int.*, *124*, 57–74, doi:10.1111/j.1365-246X.1996.tb06352.x.

Hounslow, M. W., and A. C. Morton (2004), Evaluation of sediment provenance using magnetic mineral inclusions in clastic silicates: Comparison with heavy mineral analysis, *Sediment. Geol.*, *171*, 13–36, doi:10.1016/j.sedgeo.2004.05.008.

Itambi, A. C., T. von Dobeneck, S. Mulitza, T. Bickert, and D. Heslop (2009), Millennial-scale northwest African droughts related to Heinrich events and Dansgaard-Oeschger cycles: Evidence in marine sediments from offshore Senegal, *Paleoceanography*, *24*, PA1205, doi:10.1029/2007PA001570.

Itambi, A. C., T. von Dobeneck, M. J. Dekkers, and T. Frederichs (2010), Magnetic mineral inventory of equatorial Atlantic Ocean marine sediments off Senegal-glacial and interglacial contrast, *Geophys. J. Int.*, *183*, 163–177, doi:10.1111/j.1365-246X.2010.04736.x.

Jullien, E., et al. (2007), Low-latitude "dusty events" vs. high-latitude "icy Heinrich events", *Quat. Res.*, *68*, 379–386, doi:10.1016/j.yqres.2007.07.007.

Kakol, Z., J. Sabol, J. Stickler, and J. M. Honig (1992), Effect of low-level titanium(IV) doping on the resistivity of magnetite near the Verwey transition, *Phys. Rev. B*, *46*, 1975–1978, doi:10.1103/PhysRevB.46.1975.

Kämpf, N., and U. Schwertmann (1983), Goethite and hematite in a climosequence in southern Brazil and their application in classification of kaolinitic soils, *Geoderma*, *29*, 27–39, doi:10.1016/0016-7061(83)90028-9.

Karlin, R. (1990), Magnetic mineral diagenesis in suboxic sediments at Bettis site W-N, NE Pacific ocean, *J. Geophys. Res.*, *95*, 4421–4436, doi:10.1029/JB095iB04p04421.

Karlin, R., and S. Levi (1983), Diagenesis of magnetic minerals in recent haemipelagic sediments, *Nature*, *303*, 327–330, doi:10.1038/303327a0.

Karlin, R., M. Lyle, and G. R. Heath (1987), Authigenic magnetite formation in suboxic marine sediments, *Nature*, *326*, 490–493, doi:10.1038/326490a0.

King, J., S. K. Banerjee, J. Marvin, and Ö. Özdemir (1982), A comparison of different magnetic methods for determining the relative grain size of magnetite in natural materials: Some results from lake sediments, *Earth Planet. Sci. Lett.*, *59*, 404–419, doi:10.1016/0012-821X(82)90142-X.

Knoll, M., A. Hernández-Guerra, B. Lenz, F. López Laatzen, F. Machín, T. J. Müller, and G. Siedler (2002), The Eastern Boundary Current system between the Canary Islands and the African coast, *Deep Sea Res., Part II*, *49*, 3427–3440, doi:10.1016/S0967-0645(02)00105-4.

Kohfeld, K. E., and S. P. Harrison (2001), DIRTMAP: The geological record of dust, *Earth Sci. Rev.*, *54*, 81–114, doi:10.1016/S0012-8252(01)00042-3.

Köhler, C. M., D. Heslop, M. J. Dekkers, W. Krijgsman, D. J. J. van Hinsbergen, and T. von Dobeneck (2008), Tracking provenance change during the late Miocene in the eastern

Mediterranean using geochemical and environmental magnetic parameters, *Geochem. Geophys. Geosyst.*, *9*, Q12018, doi:10.1029/2008GC002127.

Kruiver, P. P., and H. Passier (2001), Coercivity analysis of magnetic phases in sapropel S1 related to variations in redox conditions, including an investigation of the S ratio, *Geochem. Geophys. Geosyst.*, *2*(12), 1063, doi:10.1029/2001GC000181.

Kruiver, P. P., M. J. Dekkers, and D. Heslop (2001), Quantification of magnetic coercivity components by the analysis of acquisition curves of isothermal remanent magnetisation, *Earth Planet. Sci. Lett.*, *189*, 269–276, doi:10.1016/S0012-821X(01)00367-3.

Larrasoaña, J. C., A. P. Roberts, E. J. Rohling, M. Winklhofer, and R. Wehausen (2003), Three million years of monsoon variability over the northern Sahara, *Clim. Dyn.*, *21*, 689–698, doi:10.1007/s00382-003-0355-z.

Lean, C. M. B., and I. N. McCave (1998), Glacial to interglacial mineral magnetic and palaeoceanographic changes at Chatham Rise, SW Pacific Ocean, *Earth Planet. Sci. Lett.*, *163*, 247–260, doi:10.1016/S0012-821X(98)00191-5.

Liu, Q., Y. Yu, J. Torrent, A. P. Roberts, Y. Pan, and R. Zhu (2006), Characteristic low-temperature magnetic properties of aluminous goethite [α-(Fe, Al)OOH] explained, *J. Geophys. Res.*, *111*, B12S34, doi:10.1029/2006JB004560.

Lowrie, W., and F. Heller (1982), Magnetic properties of marine limestones, *Rev. Geophys.*, *20*, 171–192, doi:10.1029/RG020i002p00171.

Lyons, R., F. Oldfield, and E. Williams (2010), Mineral magnetic properties of surface soils and sands across four North African transects and links to climatic gradients, *Geochem. Geophys. Geosyst.*, *11*, Q08023, doi:10.1029/2010GC003183.

Maher, B. A. (1986), Characterisation of soils by mineral magnetic measurements, *Phys. Earth Planet. Inter.*, *42*, 76–92, doi:10.1016/S0031-9201(86)80010-3.

Maher, B. A., and R. Thompson (1992), Paleoclimatic significance of the mineral magnetic record of the Chinese loess and paleosols, *Quat. Res.*, *37*, 155–170, doi:10.1016/0033-5894(92)90079-X.

Maher, B. A., S. J. Watkins, G. Brunskill, J. Alexander, and C. R. Fielding (2009), Sediment provenance in a tropical fluvial and marine context by magnetic 'fingerprinting' of transportable sand fractions, *Sedimentology*, *56*, 841–861, doi:10.1111/j.1365-3091.2008.00999.x.

Mahowald, N., K. Kohfeld, M. Hansson, Y. Balkanski, S. P. Harrison, I. C. Prentice, M. Schulz, and H. Rodhe (1999), Dust sources and deposition during the last glacial maximum and current climate: A comparison of model results with paleodata from ice cores and marine sediments, *J. Geophys. Res.*, *104*, 15,895–15,916, doi:10.1029/1999JD900084.

Mittelstaedt, E. (1991), The ocean boundary along the northwest African coast: Circulation and oceanographic properties at the sea surface, *Prog. Oceanogr.*, *26*, 307–355, doi:10.1016/0079-6611(91)90011-A.

Mohamed, K. J., D. Rey, B. Rubio, M. J. Dekkers, A. P. Roberts, and F. Vilas (2011), Onshore-offshore gradient in reductive early diagenesis in coastal marine sediments of the Ria de Vigo, Northwest Iberian Peninsula, *Cont. Shelf Res.*, *31*, 433–447, doi:10.1016/j.csr.2010.06.006.

Moskowitz, B. M., R. B. Frankel, and D. A. Bazylinski (1993), Rock magnetic criteria for the detection of biogenic magnetite, *Earth Planet. Sci. Lett.*, *120*, 283–300, doi:10.1016/0012-821X(93)90245-5.

Mulitza, S., M. Prange, J. B. Stuut, M. Zabel, T. von Dobeneck, A. C. Itambi, J. Nizou, M. Schulz, and G. Wefer (2008), Sahel megadroughts triggered by glacial slowdowns of Atlantic meridional overturning, *Paleoceanography*, *23*, PA4206, doi:10.1029/2008PA001637.

Mullender, T. A. T., A. J. van Velzen, and M. J. Dekkers (1993), Continuous drift correction and separate identification of ferrimagnetic and paramagnetic contributions in thermomagnetic runs, *Geophys. J. Int.*, *114*, 663–672, doi:10.1111/j.1365-246X.1993.tb06995.x.

Nowaczyk, N. R. (2011), Dissolution of titanomagnetite and sulphidization in sediments from Lake Kinneret, Israel, *Geophys. J. Int.*, *187*, 34–44, doi:10.1111/j.1365-246X.2011.05120.x.

Özdemir, Ö., D. J. Dunlop, and B. M. Moskowitz (1993), The effect of oxidation on the Verwey transition in magnetite, *Geophys. Res. Lett.*, *20*, 1671–1674, doi:10.1029/93GL01483.

Passier, H. F., G. J. De Lange, and M. J. Dekkers (2001), Magnetic properties and geochemistry of the active oxidation front and the youngest sapropel in the eastern Mediterranean Sea, *Geophys. J. Int.*, *145*, 604–614, doi:10.1046/j.0956-540x.2001.01394.x.

Petermann, H., and U. Bleil (1993), Detection of live magnetotactic bacteria in South Atlantic deep-sea sediments, *Earth Planet. Sci. Lett.*, *117*, 223–228, doi:10.1016/0012-821X(93)90128-V.

Peters, C., and M. J. Dekkers (2003), Selected room temperature magnetic parameters as a function of mineralogy, concentration and grain size, *Phys. Chem. Earth, Parts A, B, and C*, *28*, 659–667, doi:10.1016/S1474-7065(03)00120-7.

Petersen, N., and H. Vali (1987), Observation of shrinkage cracks in ocean floor titanomagnetites, *Phys. Earth Planet. Inter.*, *46*, 197–205, doi:10.1016/0031-9201(87)90182-8.

Petersen, N., T. von Dobeneck, and H. Vali (1986), Fossil bacterial magnetite in deep-sea sediments from the South Atlantic Ocean, *Nature*, *320*, 611–615, doi:10.1038/320611a0.

Petrovský, E., P. Hejda, T. Zelinka, V. Kropácek, and J. Subrt (1993), Experimental determination of magnetic interactions within a system of synthetic haematite particles, *Phys. Earth Planet. Inter.*, *76*, 123–130, doi:10.1016/0031-9201(93)90061-D.

Prins, M. (1999), *Pelagic, Hemipelagic and Turbidite Depostion in the Arabian Sea During the Late Quarternary*, Univ. Utrecht, Utrecht, Netherlands.

Pye, K. (1987), *Aeolian Dust and Dust Deposits*, 334 pp., Academic, London.

Reimer, P. J., et al. (2009), IntCal09 and Marine09 radiocarbon age calibration curves, 0–50,000 years cal BP, *Radiocarbon*, *51*, 1111–1150.

Reynolds, R. L., M. L. Tuttle, C. A. Rice, N. S. Fishman, J. A. Karachewski, and D. M. Sherman (1994), Magnetization and geochemistry of greigite-bearing Cretaceous strata, North Slope basin, Alaska, *Am. J. Sci.*, *294*, 485–528, doi:10.2475/ajs.294.4.485.

Riedinger, N., K. Pfeifer, S. Kasten, J. F. L. Garming, C. Vogt, and C. Hensen (2005), Diagenetic alteration of magnetic signals by anaerobic oxidation of methane related to a change in sedimentation rate, *Geochim. Cosmochim. Acta*, *69*, 4117–4126, doi:10.1016/j.gca.2005.02.004.

Ritchie, J. C., C. H. Eyles, and C. V. Haynes (1985), Sediment and pollen evidence for an early to mid-Holocene humid period in the eastern Sahara, *Nature*, *314*, 352–355, doi:10.1038/314352a0.

Roberts, A. P., and G. M. Turner (1993), Diagenetic formation of ferrimagnetic iron sulphide minerals in rapidly deposited marine sediments, South Island, New Zealand, *Earth Planet. Sci. Lett.*, *115*, 257–273, doi:10.1016/0012-821X(93)90226-Y.

Roberts, A. P., F. Florindo, G. Villa, L. Chang, L. Jovane, S. M. Bohaty, J. C. Larrasoaña, D. Heslop, and J. D. Fitz

Gerald (2011a), Magnetotactic bacterial abundance in pelagic marine environments is limited by organic carbon flux and availability of dissolved iron, *Earth Planet. Sci. Lett.*, *310*, 441–452, doi:10.1016/j.epsl.2011.08.011.

Roberts, A. P., E. J. Rohling, K. M. Grant, J. C. Larrasoaña, and Q. Liu (2011b), Atmospheric dust variability from Arabia and China over the last 500,000 years, *Quat. Sci. Rev.*, *30*, 3537–3541, doi:10.1016/j.quascirev.2011.09.007.

Robertson, D. J., and D. E. France (1994), Discrimination of remanence-carrying minerals in mixtures, using isothermal remanent magnetisation acquisition curves, *Phys. Earth Planet. Inter.*, *82*, 223–234, doi:10.1016/0031-9201(94)90074-4.

Robinson, S. G., J. T. S. Sahota, and F. Oldfield (2000), Early diagenesis in North Atlantic abyssal plain sediments characterized by rock-magnetic and geochemical indices, *Mar. Geol.*, *163*, 77–107, doi:10.1016/S0025-3227(99)00108-5.

Rowan, C. J., A. P. Roberts, and T. Broadbent (2009), Reductive diagenesis, magnetite dissolution, greigite growth and paleomagnetic smoothing in marine sediments: A new view, *Earth Planet. Sci. Lett.*, *277*, 223–235, doi:10.1016/j.epsl.2008.10.016.

Sarnthein, M., G. Tetzlaff, B. Koopmann, K. Wolter, and U. Pflaumann (1981), Glacial and interglacial wind regimes over the eastern subtropical Atlantic and North-West Africa, *Nature*, *293*, 193–196, doi:10.1038/293193a0.

Sarnthein, M., et al. (2001), Fundamental modes and abrupt changes in North Atlantic circulation and climate over the last 60 ky - Concepts, reconstruction, and numerical modelling, in *The Northern North Atlantic: A Changing Environment*, edited by P. Schäfer et al., pp. 365–410, Springer, Berlin, doi:10.1007/978-3-642-56876-3_21.

Schmidt, A. M., T. von Dobeneck, and U. Bleil (1999), Magnetic characterization of Holocene sedimentation in the South Atlantic, *Paleoceanography*, *14*, 465–481, doi:10.1029/1999PA900020.

Schwertmann, U., and R. M. Taylor (1989), Iron oxides, in *Minerals in Soil Environments*, *Soil Sci. Soc. Am. Book Ser.*, *7*, 323–366.

Seidov, D., and M. Maslin (1999), North Atlantic deep water circulation collapse during Heinrich events, *Geology*, *27*, 23–26, doi:10.1130/0091-7613(1999)027<0023:NADWCC>2.3.CO;2.

Shackleton, N. J., M. A. Hall, and E. Vincent (2000), Phase relationships between millennial-scale events 64,000–24,000 years ago, *Paleoceanography*, *15*, 565–569, doi:10.1029/2000PA000513.

Smirnov, A. V., and J. A. Tarduno (2000), Low-temperature magnetic properties of pelagic sediments (Ocean Drilling Program Site 805C): Tracers of maghemitization and magnetic mineral reduction, *J. Geophys. Res.*, *105*, 16,457–16,471, doi:10.1029/2000JB900140.

Spassov, S., F. Heller, R. Kretzschmar, M. E. Evans, L. P. Yue, and D. K. Nourgaliev (2003), Detrital and pedogenic magnetic mineral phases in the loess/palaeosol sequence at Lingtai (Central Chinese Loess Plateau), *Phys. Earth Planet. Inter.*, *140*, 255–275, doi:10.1016/j.pepi.2003.09.003.

Stocker, T. F., and D. G. Wright (1991), Rapid transitions of the ocean's deep circulation induced by changes in surface water fluxes, *Nature*, *351*, 729–732, doi:10.1038/351729a0.

Stoner, J. S., J. E. T. Channell, and C. Hillaire-Marcel (1996), The magnetic signature of rapidly deposited detrital layers from the Deep Labrador Sea: Relationship to North Atlantic Heinrich layers, *Paleoceanography*, *11*, 309–325, doi:10.1029/96PA00583.

Stuut, J.-B., M. Zabel, V. Ratmeyer, P. Helmke, E. Schefuß, G. Lavik, and R. Schneider (2005), Provenance of present-day eolian dust collected off NW Africa, *J. Geophys. Res.*, *110*, D04202, doi:10.1029/2004JD005161.

Tarduno, J. A., and S. L. Wilkison (1996), Non-steady state magnetic mineral reduction, chemical lock-in, and delayed remanence acquisition in pelagic sediments, *Earth Planet. Sci. Lett.*, *144*, 315–326, doi:10.1016/S0012-821X(96)00174-4.

Tomczak, M. (2003), *Regional Oceanography: An Introduction*, Daya Publ. House, Delhi.

Vali, H., T. von Dobeneck, G. Amarantidis, O. Förster, G. Morteani, L. Bachmann, and N. Petersen (1989), Biogenic and lithogenic magnetic minerals in Atlantic and Pacific deep sea sediments and their paleomagnetic significance, *Geol. Rundsch.*, *78*, 753–764, doi:10.1007/BF01829320.

Vasiliev, I., M. J. Dekkers, W. Krijgsman, C. Franke, C. G. Langereis, and T. A. T. Mullender (2007), Early diagenetic greigite as a recorder of the palaeomagnetic signal in Miocene–Pliocene sedimentary rocks of the Carpathian foredeep (Romania), *Geophys. J. Int.*, *171*, 613–629, doi:10.1111/j.1365-246X.2007.03560.x.

von Dobeneck, T., N. Petersen, and H. Vali (1987), Bakterielle Magnetofossilien, *Geowiss. Unserer Zeit*, *1*, 27–55.

Weltje, G. (1997), End-member modeling of compositional data: Numerical-statistical algorithms for solving the explicit mixing problem, *Math. Geol.*, *29*, 503–549, doi:10.1007/BF02775085.

Weltje, G. J., and M. A. Prins (2007), Genetically meaningful decomposition of grain-size distributions, *Sediment. Geol.*, *202*, 409–424, doi:10.1016/j.sedgeo.2007.03.007.

White, F. (1983), *Vegetation of Africa: A Descriptive Memoir to Accompany the UNESCO/AETFAT/UNSO Vegetation Map of Africa*, *Nat. Resour. Res.*, *20*, 356 pp.

Zhang, Y. G., J. Ji, W. L. Balsam, L. Liu, and J. Chen (2007), High resolution hematite and goethite records from ODP 1143, South China Sea: Co-evolution of monsoonal precipitation and El Niño over the past 600,000 years, *Earth Planet. Sci. Lett.*, *264*, 136–150, doi:10.1016/j.epsl.2007.09.022.